

Advances in Two-Dimensional and Three-Dimensional Computer Vision

Michael A. Sutton, Stephen R. McNeill, Jeffrey D. Helm, and Yuh J. Chao

Department of Mechanical Engineering, University of South Carolina
Columbia, SC 29208, USA
sutton@sc.edu

Abstract. The foundations of two- and three-dimensional image correlation, as well as recent developments, are described in detail. The versatility and robustness of these methods are illustrated through application examples from diverse areas including fracture mechanics, biomechanics, constitutive property measurement in complex materials, model verification for large, flawed structures and non-destructive evaluation. A detailed description of experimental and data-reduction procedures is presented for the application of the two-dimensional image-correlation method to thin-sheet mixed-mode I/II fracture studies, local crack-closure measurements using optical microscopy and the measurement of constitutive properties. Application examples using three-dimensional image correlation include profiling of components for reverse engineering and manufacturing and the measurement of full-field surface deformation during wide cracked panel tensile tests for verification of buckling and crack-growth models. Results from nearly sixteen years of use have demonstrated that both two-dimensional and three-dimensional image-correlation methods are robust and accurate tools for deformation measurements in a variety of applications. The range of uses for the two- and three-dimensional image-correlation methods is growing rapidly as scientists and engineers begin to understand their true capabilities.

1 Introduction

Computer vision is a broad term, referring to a wide range of engineering applications from robotic vision to object recognition. In this review, the term computer vision will refer to computer-based, non-contacting, surface deformation measurement methods used for the study of solid structures. Even with this restriction, a wide variety of methods have been advanced in recent years, and the pace of development continues to increase rapidly. This introduction will present a brief survey of current computer-vision methods. Emphasis will be placed on recent work in the area of in-plane deformation measurement of planar surfaces using digital image correlation (DIC-2D) and the use of digital image correlation for the measurement of general deformation of planar and curved surfaces in three-dimensional space (DIC-3D).

One of the earliest papers to propose the use of computer-based analysis for deformation measurements was written by *Peters* and *Ranson* [1] in 1981. Interestingly, the original application envisioned was for analyzing images of

internal structure obtained by using ultrasonic waves. Their work described how digital ultrasound images of a solid, subjected to two-dimensional loading, could be analyzed to determine the average, through-thickness planar displacements and displacement gradients for an object. They proposed to obtain full-field measurements by comparing the locations of small regions, referred to as subsets, in a digital image of an object before loading to the subset's location in a later image of the object while under load. In their paper [1], they stated that fundamental continuum-mechanics concepts governing the deformation of small areas would be ideally suited to the development of numerical algorithms. Over the next ten years, the concepts proposed in their work have been modified, for use with optical illumination and image acquisition numerical algorithms developed [2,3,4,5,6,7,8] and the method applied successfully to the measurement of the in-plane components of surface deformations [9,10,11,12,13,14,15,16,17,18,19,20,21,22,23,24,25,26,27,28].

Among the early papers, three are of particular significance. First, in the work of *Chu* et al. [8], a description of the basic theory was outlined and experimental results were presented which conclusively demonstrated that the method could be used to accurately measure simple deformations of a solid body. Secondly, a series of papers by *Sutton* et al. [4,5] presented a new approach for determining surface deformations employing Newton-Raphson methods for optimization. The resulting method, which remains the foundation of DIC-2D to this day, resulted in a twenty-fold increase in speed with no loss in accuracy. Finally, modeling work performed by *Sutton* et al. [3] demonstrated that the primary parameters affecting the accuracy of the surface deformations obtained by the Newton-Raphson based DIC-2D method are (a) the number of quantization levels in the digitization process (i.e. the number of bits in the A/D converter for converting light intensity into a digital value), (b) the ratio of the sampling frequency to the frequency of the intensity signal (i.e. the number of sensors in the camera used to record a given pattern) and (c) use of interpolation functions to reconstruct the intensity pattern at sub-pixel locations.

Researchers continued to improve and gain a deeper understanding of the DIC-2D method, and others began using the method to address a wide range of problems [9,10,11,12,13,14,15,16,17,18,19,20,21,22,23,24,25,26,27,28]. DIC-2D was applied to the measurement of velocity fields both in two-dimensional seeded flows [9] and in rigid-body mechanics [11]. DIC-2D principles were used successfully to measure strain fields in retinal tissue overcoming the difficulties inherent in measuring strains in flexible materials and to determine the tissue's mechanical properties under monotonic and cyclic loading [13,15]. The non-contacting nature of DIC-2D also allowed the measurement of strains in thin paper specimens [16] by researchers at the University of South Carolina. Most significantly, the DIC-2D method continues to be used extensively in fracture-mechanics studies [10,14,19,20,21,22,23,24,25,26], including measurement of (a) strain fields near stationary and growing crack-tips [22,23,24],

(b) crack-tip opening displacement during crack growth [25,26,27,28] and (c) strain measurements near crack-tips at high temperatures [31,32]. Recently, the method has been successfully extended to the study of deformations from scanning tunneling electron microscopy images [33,34,35] as well as deformation in concrete during compressive loading [36].

It is worth noting that the paper by *Chao et al.* [16] has led to the adoption of the DIC-2D method by many researchers in the wood, paper and forest products area. The method has been used to (a) study the deformation of single wood cells [37], (b) determine the mechanical properties of small specimens made of wood products [38,39,40] and ASTM standard-sized wood/wood composite specimens [41,42,43,44], (c) study the drying process in wood specimens [45,46,47] and (d) determine the mechanical properties of wooden connections [48,49].

Though all of the applications described above employ DIC-2D concepts, including the use of direct image-correlation principles for determination of displacements and displacement gradients, Fast Fourier Transforms [29,30] (FFT's) were shown to be a viable alternative for those applications where in-plane strains and rigid body rotations are relatively small. The FFT method uses discrete Fourier transforms of the intensity pattern in both deformed and undeformed sub-regions to determine the cross-correlation function. The displacement of the deformed sub-region is then estimated by locating the peak of the cross-correlation function. The FFT approach was found to be both fast and accurate for a large number of applications. However, the method does not allow subset deformation and hence experiences a loss of accuracy, even in the presence of only moderate strains or in-plane rotations. Applications have included determination of deformations in shock mounts and the mechanical properties of both fibers and the fiber-matrix interface region in a composite using images from an scanning electron microscope (SEM).

One fundamental limitation of both the DIC-2D and FFT methods is their basis in two-dimensional concepts. The change in magnification due to a relatively small out-of-plane motion, can introduce significant errors in the measured in-plane displacement. To minimize these effects, *Sutton et al.* [22,23,24] utilized an optical system that is relatively insensitive to small magnitudes of out-of-plane motion. This insensitivity was achieved by increasing the distance from the camera to the surface of the object, requiring the use of long-focal-length lenses, and thereby minimizing any change in magnification due to small out-of-plane movements of the object. Long-focal-length lens systems continue to be used successfully, including the use of a far-field microscope to measure crack-tip opening displacements within a few micrometers of the crack-tip [50,51] during cyclic loading to quantify crack-closure effects. Attempts to correct for large out-of-plane movements have proven extremely difficult if not impossible. For example, early attempts by *Peters et al.* [19] to correct the in-plane deformations using approximate estimates of the out-of-plane motion for a pressurized cylinder were not successful.

In addition, early work in the paper industry [53] attempted to infer out-of-plane buckling from the “measured” in-plane deformations using the DIC-2D system with minimal success. More recently, *Lu et al.* [52] have shown that correcting the “measured” displacements for nominally cylindrical specimens will result in strain errors of the order of 2000 μ strain. These limitations provided the motivation to develop a method to measure full three-dimensional displacements.

The first three-dimensional displacement measurements were performed in 1988 by McNeill and resulted in an unpublished internal report [54]. Using a known horizontal translation of one camera to obtain two views of an object, McNeill calibrated a simple stereo vision system and demonstrated that the shape of an inclined planar object could be accurately measured. In 1991, *Luo et al.* [55] successfully developed a two-camera stereo vision system for deformation measurements and applied it to fracture problems [56,57]. To overcome some of the key limitations of the method (square subsets that remained square in both cameras, mismatch in the triangulation of corresponding points, and a calibration process that was laborious and time-consuming), *Helm et al.* [58,59] successfully developed a two-camera stereo vision system that (a) included the effects of perspective on subset shape (b) constrained the analysis to epipolar lines and (c) simplified the process of calibrating the system. The measurement system, 3D Digital Image Correlation (DIC-3D), is being used for a wide range of applications to both large and small structures.

In Sect. 2, the theory for DIC-2D and DIC-3D will be described. In Sect. 3, recent applications of both DIC-2D and DIC-3D will be presented. In Sect. 4, a discussion of the advantages and disadvantages of the DIC-2D and DIC-3D methods is provided. In Sect. 5, a summary of recent advances will be given, as well as a discussion of future applications that are envisioned.

2 Theory and Numerical Implementation

2.1 Two-Dimensional Video Image Correlation

2.1.1 Basic Concepts

The basis of two-dimensional video image correlation for the measurement of surface displacements is the matching of one point from an image of an object’s surface before loading (the undeformed image) to a point in an image of the object’s surface taken at a later time/loading (the deformed image). Assuming a one-to-one correspondence between the deformations in the image recorded by the camera and the deformations of the surface of the object, an accurate, point-to-point mapping from the undeformed image to the deformed image will allow the displacement of the object’s surface to be measured. Two main requirements must be met for the successful use of DIC-2D. First, in order to provide features for the matching process, the surface of the object must have a pattern that produces varying intensities of diffusely reflected

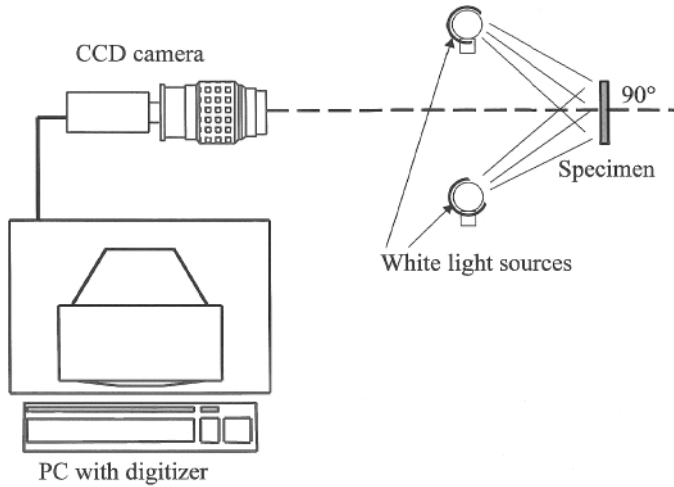


Fig. 1. Schematic of a data-acquisition system for two-dimensional video image correlation

light from its surface. This pattern may be applied to the object or it may occur naturally. Secondly, the imaging camera must be positioned so that its sensor plane is parallel to the surface of the planar object, as shown in Fig. 1.

The imaging process of the camera converts the continuous intensity field reflected from the surface $O(X, Y)$ into a discrete field $I(X, Y)$ of integer intensity levels. In a CCD camera, this transformation occurs when the light incident on a sensor (commonly known as a pixel) is integrated over a fixed time period. The rectangular array of sensors in a charge-coupled device (CCD) array converts the continuous intensity pattern into a discrete array of integer intensity values, $I(i, j)$, where i denotes the row number and j denotes the column number in the sensor plane. The displacement field for an object is obtained at a discrete number of locations by choosing subsets from the initial image and searching throughout the second image to obtain the optimal match. Details of this process are outlined in the following paragraphs.

The process of deformation in two dimensions is shown schematically in Fig. 2. The functions are defined as follows; (a) $O(X, Y)$ denotes the continuous intensity pattern for the undeformed object, (b) $O'(X, Y)$ is the continuous intensity pattern for the deformed object, (c) $I(X, Y)$ is the discretely sampled intensity pattern for the undeformed object and (d) $I'(X, Y)$ is the discretely sampled intensity pattern for the deformed object. It is important to note that a basic tenet of the DIC-2D method is that points in $I(X, Y)$ and $I'(X, Y)$ are assumed to be in one-to-one correspondence with points in $O(X, Y)$ and $O'(X, Y)$, respectively. Thus, one can use $I(X, Y)$ and $I'(X, Y)$ to determine the displacement field for the object $O(X, Y)$.

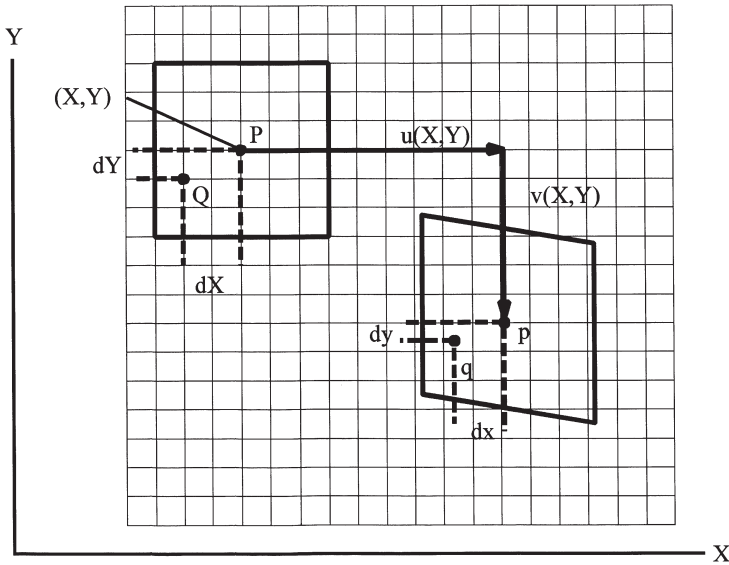


Fig. 2. Schematic of the deformation process in two dimensions

Recalling basic continuum-mechanics concepts for the deformation of a region, one would expect that the object point imaged onto the center of an integer pixel location in the undeformed image will be imaged to locations between pixels of the stationary CCD camera after deformation. Thus, obtaining accurate estimates for surface deformations using $I(X, Y)$ and $I'(X, Y)$ requires an interpolation scheme to reconstruct a continuous intensity function. The intensity pattern for a typical 10×10 pixel subset is shown in Fig. 3, where black and white represent low and high intensity, respectively. A wide variety of interpolation methods has been used successfully and Fig. 4 shows a plot of the raw intensity data, bilinear interpolation fit, bicubic interpolation fit and a bicubic-spline fit for the 10×10 -subset shown in Fig. 3.

It is noted that accurate measurement of surface deformations requires that the mapping from the undeformed image to the deformed image be as accurate as possible. Thus, it is important to “oversample” the intensity pattern, using several sensors to sample each feature of the intensity pattern. Through a combination of oversampling, interpolation and quantization with at least 8 bits, the original intensity pattern can be reconstructed with reasonable accuracy and the displacement field estimated with accuracy of ± 0.02 pixels or better.

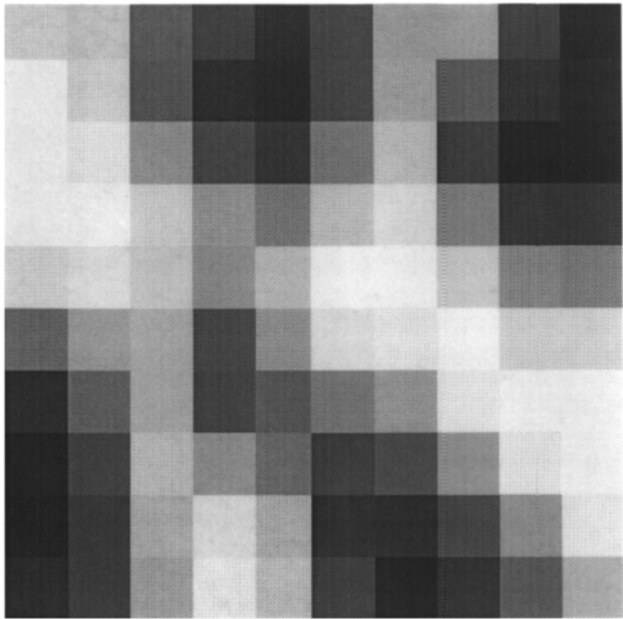


Fig. 3. Intensity values for a typical 10×10 pixel subset

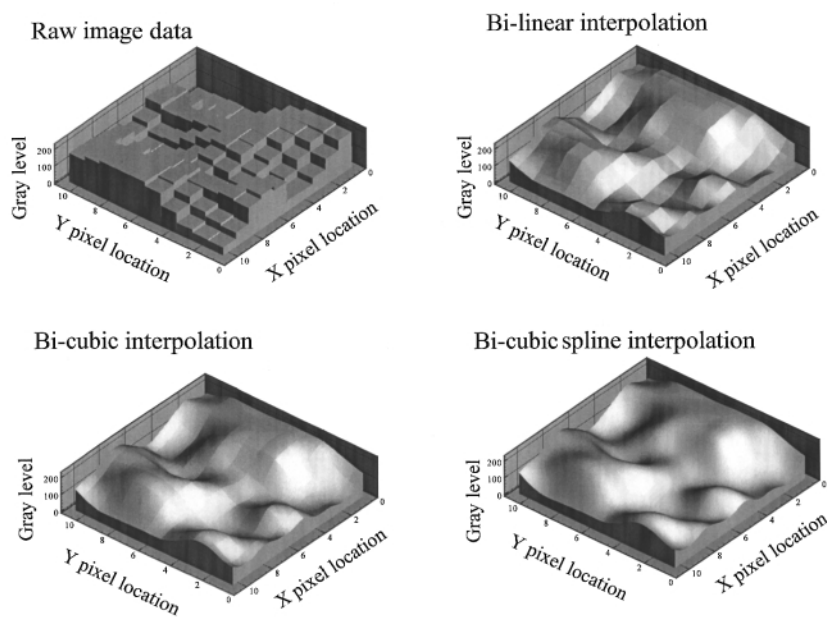


Fig. 4. Four representations of the intensity values over the 10×10 pixel region

2.1.2 Two-Dimensional Image Correlation: Mathematical Formulation

For the small subset centered at (X, Y) on the undeformed object in Fig. 2, the discretely sampled and continuously interpolated intensity pattern at points P and Q, located at positions (X, Y) and $(X+dX, Y+dY)$ respectively, can be written as

$$\begin{aligned} I(P) &= I(X, Y) , \\ I(Q) &= I(X + dX, Y + dY) , \end{aligned} \quad (1)$$

where (dX, dY) represent small distances in the (X, Y) coordinate system. Note that, if the values for dX and dY are integer pixel values, then no interpolation is required for the undeformed image. As shown in Fig. 2, after deformation of an object, points P and Q are deformed into positions p and q, respectively. Assuming that the intensity pattern recorded after deformation is related to the undeformed pattern by the object deformations, and defining $\{u(X, Y), v(X, Y)\}$ as the displacement vector field, we can write $x = X + u(X, Y)$, $y = Y + v(X, Y)$ so that

$$\begin{aligned} I'(x, y) &= I(X + u(X, Y), Y + v(X, Y)) , \\ I'(x + dx, y + dy) &= I[X + dX + u(X + dX, Y + dY), Y + dY \\ &\quad + v(X + dX, Y + dY)] , \\ &= I \left[X + u(X, Y) + \left(1 + \frac{\partial u}{\partial X} \right) dX + \frac{\partial u}{\partial Y} dY, \right. \\ &\quad \left. Y + v(X, Y) + \frac{\partial v}{\partial X} dX + \left(1 + \frac{\partial v}{\partial Y} \right) dY \right] . \end{aligned} \quad (2)$$

Assuming that the subset is sufficiently small so that the displacement gradients are nearly constant throughout the region of interest, each subset undergoes uniform strain resulting in the parallelogram shape for the deformed subset shown in Fig. 2. Conceptually, determining $u, v, \partial u/\partial X, \partial u/\partial Y, \partial v/\partial X, \partial v/\partial Y$ for each subset is simply a matter of determining all six parameters so that the intensity values at each point in the undeformed and deformed regions match. To obtain these values, there are several measures of intensity pattern correspondence that could be used, including the following summations for a series of selected points, Q_i

- (a) $\Sigma_i |I'(q_i) - I(Q_i)|$ (magnitude of intensity value difference)
- (b) $\Sigma_i (I'(q_i) - I(Q_i))^2$ (sum of squares of intensity value differences)
- (c) $\frac{\Sigma_i (I'(q_i) I(Q_i))}{(\Sigma_i I'(q_i)^2)^{\frac{1}{2}} (\Sigma_i I(Q_i)^2)^{\frac{1}{2}}}$ (normalized cross-correlation)
- (d) $\Sigma_i (I'(q_i) I(Q_i))$ (cross-correlation)

Minimization of (a,b) and maximization of (c,d) for each subset will provide the optimal estimates for all six parameters [2,4,5,8,11]. It is noted that,

when a range of values are chosen for the displacements of the centerpoint, $(u_l(P), v_l(P))$, and the displacement gradients in the subset, $\{u/\partial X, \partial u/\partial Y, \partial v/\partial X, \partial v/\partial Y\}$, the positions of the points will fall between integer values in the deformed subset. Thus, the intensity values at $M \times M$ points in the deformed subset must be obtained from the interpolation function, since non-integer locations correspond to positions that are between pixel locations. As noted previously, a wide range of interpolation methods have been used successfully, including bilinear, bicubic and bicubic-spline. In most of the results to be discussed in the following sections, a normalized cross-correlation function is used to obtain best estimates for the displacement field and it is defined as

$$1.0 - C_l(u, v, \partial u/\partial X, \partial u/\partial Y, \partial v/\partial X, \partial v/\partial Y) = 1.0 - \frac{\sum_{i=1}^{i=N} \sum_{j=1}^{j=M} I(X_i, Y_j) I'[X_i + u(X_i, Y_j), Y_j + v(X_i, Y_j)]}{\sum_{i=1}^{i=N} \sum_{j=1}^{j=M} \{I^2(X_i, Y_j) I'^2[X_i + u(X_i, Y_j), Y_j + v(X_i, Y_j)]\}^{\frac{1}{2}}} \cdot (3)$$

The values for $u(P), v(P), \partial u/\partial X, \partial u/\partial Y, \partial v/\partial X, \partial v/\partial Y$ which minimizes the quantity $(1.00 - C_l)$ are assumed to represent the best estimates of the subset's displacement and strain components. It is noted that the quantity $(1.00 - C_l)$ is zero for a perfect match and one for orthogonal (completely mismatched) patterns, providing a quantitative measure of the accuracy of the match between deformed and undeformed subsets. A wide range of optimization methods has been used successfully to obtain the optimal value for $(1.00 - C_l)$, including Newton-Raphson [2,3,4,5,7,8], coarse-fine [2,3,4,5] and recently the Levenburg-Marquardt method. Currently, most of the analyses are performed with the Newton-Raphson method, since it is at least twenty times faster than the coarse-fine search. Recent analyses performed using the Levenburg-Marquardt method indicate that this method is as fast as the Newton-Raphson approach and has better convergence characteristics.

To obtain optimal estimates for all six parameters in (3), the iteration process is as follows:

1. Obtain an initial estimate of centerpoint translation for the subset of interest from visual inspection of the images, denoting it as $[u_l(P), v_l(P)]$,
2. Allow the gradients to be non-zero and perform a full, six-parameter search process to minimize (3). The values of u, v and the displacement gradients which minimize $(1 - C_l)$ are the optimal estimates for the displacements and displacement gradients,
3. Using results from the previous subset as the initial guess, repeat (2) for the next subset,
4. Repeat steps (2) and (3) until data is obtained throughout the region of interest.

With regard to accuracy of the parameters obtained by this method, several points should be noted:

- (a) Local gradient terms for each subset vary by ± 0.005 in a uniform strain region due to a combination of factors including interpolation errors, quantization levels and noise in the intensity pattern. Due to this, gradients for each subset are only used to improve estimates of the centerpoint displacement $[u_l(P), v_l(P)]$.
- (b) By obtaining the displacements of many subset centers, P_I , a displacement field is generated. Typical errors are ± 0.02 pixels for each displacement component. The data field is smoothed using one of many techniques available [7,60,61] to reduce noise in the measured displacement fields. Using 8-bit digitizers and bilinear interpolation, typical point-to-point accuracy in the displacement gradients obtained from smoothed displacement data is $\pm 200 \times 10^{-6}$ in a non-uniform strain field.
- (c) With regard to surface fitting, bilinear interpolation is the simplest approach for estimating intensity values between pixel locations. It has been used effectively in a wide range of applications. However, previous experiments have shown that bicubic and bicubic-spline interpolation methods provide improved accuracy, especially when the displacement gradients are small (e.g. displacement gradients < 0.002 throughout the image area).
- (d) The use of zero gradients for all subsets to obtain a displacement field is computationally efficient. For small-strain cases, the choice of zero displacement gradients has no discernible bias and gives reasonable accuracy (typical accuracy in strains is ± 200 strain). However, for strain or rotation of the order of 0.03, errors in the measured displacements in using this approach will increase rapidly and the use of local displacement gradients is recommended.

Equations (1,2,3) define a procedure for obtaining the optimal affine transformation between an undeformed and deformed image pair under the restrictions imposed on the transformation by continuum-mechanics principles. A similar procedure is commonly used in computer graphics as part of an image “warping” process [62], where the transformations are generally not restricted by continuum requirements.

With regard to the various correlation formulae described above, the following remarks are to be noted. First, all forms have been used successfully by the authors to determine the optimal affine transformation for a subset. However, the sum of squares of differences, the sum of magnitude of differences and the cross-correlation have two disadvantages. First, all are somewhat sensitive to changes in lighting, with errors in the measured displacements increasing as both contrast and background intensity levels change. Secondly, since the correlation coefficient increases substantially as lighting changes occur, it is difficult to determine whether accurate pattern matches have been obtained. For these reasons, we have used the normalized cross-correlation (3) in all of our analyses. Our studies have shown that (3) can be used to obtain optimal affine transformation parameters with background lighting changes

up to 30%. Furthermore, the normalized correlation coefficient obtained during the analysis can be used to determine when “matching” has degraded.

With regard to the accuracy of DIC-2D relative to other approaches, it is noted that *James* [63] has developed a digital image-processing methodology for estimating in-plane displacements from SEM and optical photomicrographs. Typically, the error in each displacement for his work is ± 0.50 pixels. However, due to the large magnification factors associated with the photomicrograph ($5000\times$), the dimensional error in displacement can be as low as $0.10\text{ }\mu\text{m}$. For comparison, using a 2400 line/mm grating in moiré interferometry, Post [64] has shown that the displacement sensitivity of the method is of the order of $0.42\text{ }\mu\text{m}$ with accuracy in strain of approximately $50\text{ }\mu\text{strain}$. However, *McKelvie* [65] noted that lens aberrations and the loss of frequency information due to the finite lens size might limit the actual displacement sensitivity to about five grating pitches or a displacement error of $\pm 2\text{ }\mu\text{m}$.

2.1.3 Calibration Process for DIC-2D System

In general, calibration of a DIC-2D system would require a process that is somewhat similar to the procedure outlined in Sect. 2.2.2 and 2.2.3 for three-dimensional vision. One major difference is that, for two-dimensional calibration, *in-plane translations and/or rotations* are performed for the planar object to determine (a) the aspect ratio λ (ratio of the row and column dimensions for each sensor in the camera), which is constant for a specific camera-digitizing board interface, (b) the magnification factor for one direction in pixels/mm, (c) the location of the lens center, and (d) the distortion coefficient for the lens. Fortunately, if high quality lenses are used in the imaging process, the effects of image distortion can be neglected so that two-dimensional calibration requires the determination of only one magnification factor and the aspect ratio.

One method for determining the aspect ratio for a camera-digitizing board combination is to perform a series of in-plane rotation tests for a planar object having a high contrast speckle pattern. Using a least squares procedure, the location of the center of rotation, the unknown rotation angles and λ are determined. Accuracy of $\pm 5 \times 10^{-4}$ for λ has been obtained using this method. Another method, typically employed for DIC-3D studies where a precision-ground grid is used as part of the calibration process, is described in Sect. 2.2.3.

The magnification factors, relating the size of the region being imaged to the pixel dimensions of the sensor plane, are generally determined by one of two methods. A highly accurate method employs a series of translations for a planar surface having a high contrast speckle pattern. By performing image correlation to determine the translation in pixels, the magnification factors for both the row and column directions are obtained. Another method uses a measurement standard attached to the surface of a planar object. By performing edge detection to locate the pixel position of two marks having a

known spacing, the magnification factor can be determined with an accuracy of 0.2% in most cases.

2.2 Three-Dimensional Video Image Correlation

2.2.1 Basic Concepts

Single camera DIC systems are limited to planar specimens that experience little or no out-of-plane motion. This limitation can be overcome by the use of a second camera observing the surface from a different direction. Three-dimensional Digital Image Correlation (DIC-3D) is based on a simple binocular vision model. In principle, the binocular vision model is similar to human depth perception. By comparing the locations of corresponding subsets in images of an object's surface taken by the two cameras, information about the shape of the object can be obtained. In addition, by comparing the changes between an initial set of images and a set taken after load is applied, full-field, three-dimensional displacement can be measured. Both the initial shape measurement and the displacement measurement require accurate information about the placement and operating characteristics of the cameras being used. To obtain this information, a camera calibration process must be developed and used to accurately determine the model parameters. In the following paragraphs, key aspects of the DIC-3D method are outlined.

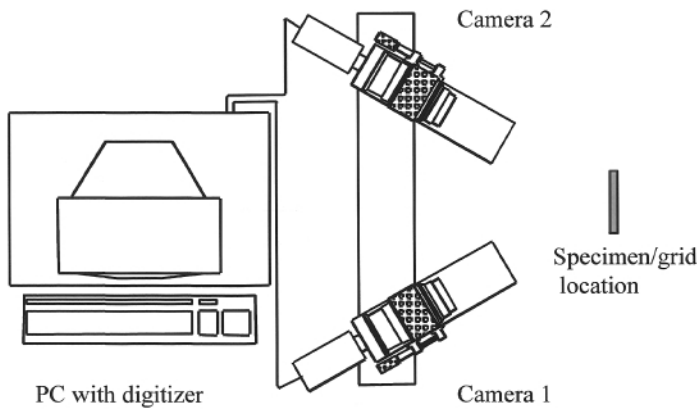


Fig. 5. Schematic of a complete three-dimensional measurement system

A schematic of a typical DIC-3D system is shown in Fig. 5. A photograph indicating typical orientations for the cameras and specimen in a DIC-3D system is shown in Fig. 6. In this work, the camera and lens system are modeled as a pin-hole device. To increase the accuracy of the pin-hole model, a correction term for Seidel lens distortion [55,56,57,58] is included. The imaging characteristics of a camera modeled in this manner can be described by

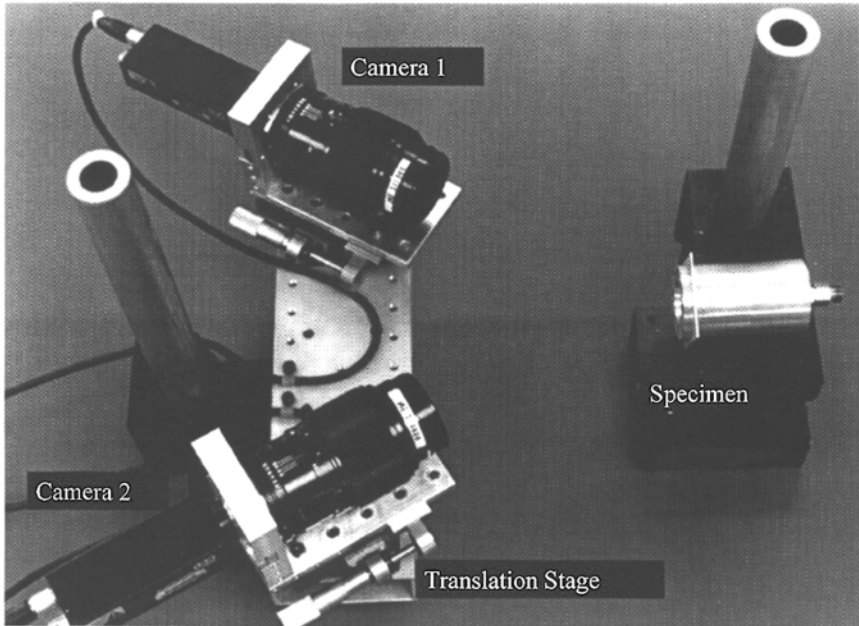


Fig. 6. Photograph of typical camera components and specimen in a three-dimensional measurement system

five parameters. The parameters are (a) the pinhole distance (phd), (b) the two-dimensional location of the intersection of the optical axis and the sensor plane, denoted as the center of the image (C_x, C_y), (c) a lens distortion factor, κ , and (d) the aspect ratio, λ . The parameters $C_x, C_y, \text{phd}, \kappa$ and λ describe the internal properties of a camera and are *intrinsic* parameters. In addition, the parameters $\alpha, \beta, \gamma, X_0, Y_0, Z_0$ describe the overall orientation and position of a camera and are *extrinsic* parameters. Thus, a total of eleven parameters are required to describe the imaging process and global orientation of each camera.

Figure 7 shows the seven coordinate systems that are used to describe the location of points both in space and on images. As shown in Fig. 7, the system-wide coordinate system ($X_{\text{sys}}, Y_{\text{sys}}, Z_{\text{sys}}$) serves as a bridge between the two cameras. Coordinates ($X_{\text{cam1}}, Y_{\text{cam1}}, Z_{\text{cam1}}$) and ($X_{\text{cam2}}, Y_{\text{cam2}}, Z_{\text{cam2}}$) describe spatial locations in the camera coordinate system for Camera 1 (cam1 system) and Camera 2 (cam2 system), respectively, with the origin of each camera system located at each camera's pinhole. The four remaining coordinate systems are used to transform positions from pixel coordinates in each camera into physical dimensions in the cam1 and cam2 systems. It should be noted that the calibration process (a) determines the position and orientation of the system-wide coordinate system ($X_{\text{sys}}, Y_{\text{sys}}, Z_{\text{sys}}$) on a calibrated grid, which also serves as the global coordinate system and (b) determines

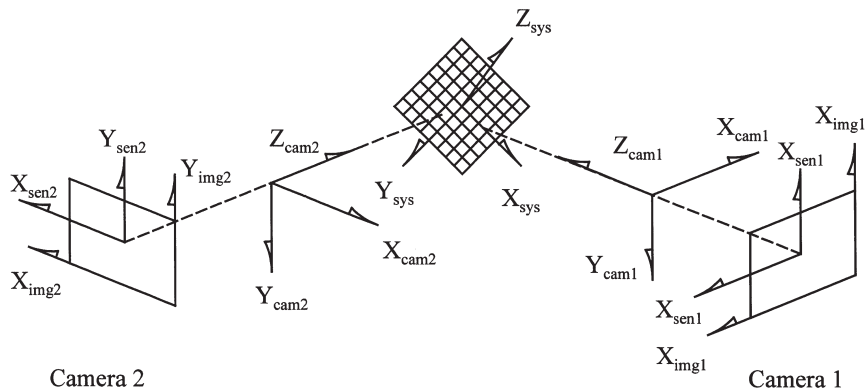


Fig. 7. Schematic of coordinate systems employed in three-dimensional measurements

the location and orientation of each camera relative to the system coordinate system.

The relationship between the camera coordinates and the system coordinates can be obtained by initially aligning the camera and system coordinate systems. Then, the rotational matrix relating these systems is obtained by consecutively rotating the system coordinate system by (a) α about Z_{cam} , (b) γ about Y_{cam} and (c) β about X_{cam} . This yields the following rotational transformation that will convert system coordinates into camera coordinates

$$[R] = \begin{bmatrix} \cos \alpha \cos \beta + \cos \alpha \sin \gamma \sin \beta & \cos \alpha \cos \beta - \sin \alpha \sin \gamma \sin \beta & \sin \gamma \\ \sin \alpha \cos \beta + \cos \alpha \sin \gamma \sin \beta & \sin \alpha \cos \beta - \cos \alpha \sin \gamma \sin \beta & -\cos \gamma \sin \beta \\ \sin \alpha \sin \beta - \cos \alpha \sin \gamma \cos \beta & \cos \alpha \sin \beta + \sin \alpha \sin \gamma \cos \beta & -\cos \gamma \cos \beta \end{bmatrix} \quad (4)$$

Defining the vector $[T]$ to be the translation (X_0, Y_0, Z_0) of the origin of the system coordinates with respect to the rotated camera coordinates, one has

$$[T] = \begin{bmatrix} X_0 \\ Y_0 \\ Z_0 \end{bmatrix}. \quad (5)$$

The transformation from system to camera coordinates can be written as

$$\begin{bmatrix} X_{cam} \\ Y_{cam} \\ Z_{cam} \end{bmatrix} = [R] \begin{bmatrix} X_{sys} \\ Y_{sys} \\ Z_{sys} \end{bmatrix} + [T]. \quad (6)$$

The projection from camera coordinates to sensor coordinates can be derived from similar triangles as

$$\frac{X_{cam}}{X_{sen}} = \frac{Y_{cam}}{Y_{sen}} = \frac{Z_{cam}}{phd}, \quad (7)$$

which can be rearranged to give the following projection equations:

$$\begin{aligned} X_{\text{sen}} &= \frac{\text{phd}X_{\text{cam}}}{Z_{\text{cam}}} , \\ Y_{\text{sen}} &= \frac{\text{phd}Y_{\text{cam}}}{Z_{\text{cam}}} . \end{aligned} \quad (8)$$

Since (8) demonstrates that the projection of a known sensor coordinate into a three-dimensional position results in a one-to-many transformation, the mapping of sensor-plane positions to a unique three-dimensional location requires additional information. Thus, two cameras are most often employed to resolve the ambiguity in the mapping process.

To account for lens distortion, an approximate form for the relationship between distorted and undistorted ($X_{\text{sen}}, Y_{\text{sen}}$) locations are

$$\begin{aligned} \overline{X_{\text{sen}}} &= \frac{X_{\text{sen}}}{1 + \kappa \sqrt{X_{\text{sen}}^2 + Y_{\text{sen}}^2}} , \\ \overline{Y_{\text{sen}}} &= \frac{Y_{\text{sen}}}{1 + \kappa \sqrt{X_{\text{sen}}^2 + Y_{\text{sen}}^2}} , \end{aligned} \quad (9)$$

and an approximate inverse of (9) can be written

$$\begin{aligned} X_{\text{sen}} &= \frac{2\overline{X_{\text{sen}}}}{1 + \sqrt{1 - 4\kappa(\overline{X_{\text{sen}}}^2 + \overline{Y_{\text{sen}}}^2)}} , \\ Y_{\text{sen}} &= \frac{2\overline{Y_{\text{sen}}}}{1 + \sqrt{1 - 4\kappa(\overline{X_{\text{sen}}}^2 + \overline{Y_{\text{sen}}}^2)}} , \end{aligned} \quad (10)$$

to convert from distorted to undistorted sensor plane locations.

To access the image data stored in the computer, the sensor coordinates must be related to image coordinates. This is accomplished with a simple transformation of the sensor coordinates. This transformation requires the location of the image center (C_x, C_y) and the aspect ratio (λ) of the camera/digitizer system. The transformation from the sensor plane to the image coordinates is written

$$\begin{aligned} X_{\text{img}} &= \overline{X_{\text{sen}}} + C_x , \\ Y_{\text{img}} &= \lambda \overline{Y_{\text{sen}}} + C_y . \end{aligned} \quad (11)$$

Equations (4 - 11) relates coordinates for an object point ($X_{\text{sys}}, Y_{\text{sys}}, Z_{\text{sys}}$) to its two-dimensional position in the camera sensor plane. The DIC-3D method employs two cameras to determine three-dimensional positions of a point through use of the two-dimensional images of the same point from both cameras. It must be emphasized that accurate three-dimensional measurements

imply that (4 – 11) accurately model the imaging process. Thus, the calibration process used to determine the eleven parameters ($\alpha, \beta, \gamma, X_0, Y_0, Z_0, C_x, C_y, \text{phd}, \kappa$ and λ) in (4 – 11) for each camera in the DIC-3D system must be accurate and reliable so that three-dimensional surface measurements can be obtained with optimal accuracy.

2.2.2 Calibration Process for DIC-3D System

As noted previously, λ is solely a function of the camera-digitizing board interface and its value can be obtained independently. Furthermore, if the camera-digitizing board combination is the same for both cameras, the value obtained for λ from one camera can be used for both cameras.

After determining λ , each camera is calibrated separately to obtain the remaining ten parameters using a precision grid common to both cameras. Since both cameras are calibrated using simultaneously recorded images of the same grid (i.e. both cameras have the same system coordinate system), the positions of the cameras relative to each other are known after the calibration. As part of the calibration process for each camera, the relative position of the grid with respect to each camera must be altered at least one time. One method to achieve this goal is to translate each camera perpendicular to the sensor plane by a known distance. It is noted that several translations can be used in the calibration process, but only one translation along the direction perpendicular to the sensor plane is required.

2.2.3 Determination of Aspect Ratio, λ

To obtain an accurate value for λ , one can use the procedure outlined briefly in Sect. 2.1.3. However, in most of our DIC-3D tests, the following procedure was used. First, a precision ground grid was mounted (a) in the camera's field of view and (b) approximately perpendicular to the sensor plane. Secondly, at least twenty images are acquired. Thirdly, for each image, the sensor-plane locations for all of the grid's intersection points are determined using image thresholding and least-squares curve fitting. Fourthly, using several 5×5 square sub-group of the intersection points within each image, several average values for the ratio ($\Delta Y_{\text{img}} / \Delta X_{\text{img}}$) of alternate diagonal subset vertices in the 5×5 sub-group are obtained for each image. By averaging the N ratio values obtained from all twenty grid images, one obtains $\lambda \cong [1/N \sum_{i=1, N} (\Delta Y_{\text{img}} / \Delta X_{\text{img}_i})]$. As noted earlier, this experiment must be performed only once for a given computer-camera-digitizer combination. For a Sony XC-77 camera-Data Translation digitizing board combination, the value for λ obtained by performing these experiments is $\lambda \approx 0.9620$.

Though this value for λ can be used to obtain accurate three-dimensional displacement data, in many applications it is important to achieve optimal accuracy. One method used previously [58] to improve the accuracy in λ is as follows. First, after determining λ and calibrating the cameras (see next

section), a DIC-3D system is constructed. Secondly, a precision-ground flat plane with random pattern is placed in the field of view and translated by a known amount perpendicular to the plane. Thirdly, images are acquired and analyzed to obtain data related to the object motion. An improved value for λ is obtained that minimizes the difference between the measured planar position and the known translation over the field of view. Using this method, an improved estimate for $\lambda \approx 0.9617$ was obtained.

2.2.4 Determination of Camera Parameters

After estimating λ , the remaining ten parameters for each camera must be determined to complete the calibration process. After calibration cameras must remain in the same position relative to each other. As shown in Fig. 7, the calibration grid is positioned near the specimen location. The calibration grid establishes the position and orientation of the system coordinate system, with the initial plane of the grid defined to have $Z_{\text{sys}} = 0$. The camera system is positioned so that images of the grid can be acquired. Lighting on the grid is adjusted to produce roughly even illumination of the background, with the grid lines clearly visible. Each camera is focused on the grid using a large F -number to maximize the depth of field.

As with the determination of λ , the camera calibration process is based on a series of images of the calibration grid. The camera calibration process is as follows. First, images are acquired simultaneously by both cameras in the initial position. Secondly, both cameras are translated perpendicular to the sensor plane by ΔZ_1 and a new set of images of the grid is acquired. Thirdly, translations are repeated for several ΔZ_J and images recorded by each camera. Fourthly, intersection points for the grid are obtained using the procedure described in Sect. 2.2.3. Since the intersection points provide a series of known positions $(X_{\text{sys}}, Y_{\text{sys}}, 0)_J$, these locations form the foundation for the calibration process. Fifthly, the sensor position for all of the known grid positions is determined using a combination of (4,5,6,7)

$$Y_{\text{sen}} = \text{phd} \times \frac{(\sin \alpha \cos \beta + \cos \alpha \sin \gamma \sin \beta)X_{\text{sys}} + (\cos \alpha \cos \beta - \sin \alpha \sin \gamma \sin \beta)Y_{\text{sys}} + Y_0}{(\sin \alpha \sin \beta - \cos \alpha \sin \gamma \cos \beta)X_{\text{sys}} + (\cos \alpha \sin \beta + \sin \alpha \sin \gamma \cos \beta)Y_{\text{sys}} + Z_0 + \Delta Z_{\text{cam}}} \quad (12)$$

$$X_{\text{sen}} = \text{phd} \times \frac{\cos \alpha \cos \gamma X_{\text{sys}} - \sin \alpha \cos \gamma Y_{\text{sys}} + X_0}{(\sin \alpha \sin \beta - \cos \alpha \sin \gamma \cos \beta)X_{\text{sys}} + (\cos \alpha \sin \beta + \sin \alpha \sin \gamma \cos \beta)Y_{\text{sys}} + Z_0 + \Delta Z_{\text{cam}}} \quad (13)$$

Sixth, the $(X_{\text{sen}}, Y_{\text{sen}})_J$ positions are corrected for lens distortion and converted to image coordinates using (8,9,10,11) and the locations of the intersections in the image $(X_{\text{int}}, Y_{\text{int}})_J$ are acquired. This allows a direct comparison of the projected intersection points to the imaged positions for

each point. Seventh, the error function is written:

$$\text{Error} = \sum_{J=1}^n [(x_{\text{img}_J} - x_{\text{int}_J})^2 + (y_{\text{img}_J} - y_{\text{int}_J})^2] \quad (14)$$

and (14) is minimized for each camera in the DIC-3D system using a Levenberg-Marquardt non-linear optimization method [58,59] to establish the ten parameters for each camera.

2.2.5 Profile and 3-D Displacement Measurements

Profile measurements for an object typically use a random pattern, either projected onto or bonded to the surface. In either case, after calibration is complete, the object to be profiled is placed in the field of view and images are acquired simultaneously by both of the calibrated cameras. The process of determining the three-dimensional profile for an object is shown in Fig. 8. Since curved surfaces can be approximated by a finite number of planar patches, the image intensity values obtained from Camera 1 are projected onto a virtual plane. The plane is described in Camera 1 coordinates by two direction angles θ, ϕ and the variable distance Z_p denoting the location of the intersection of the plane and the optic axis for Camera 1. An equation for the virtual plane can be written in the form:

$$Z_p \sqrt{1 - \cos^2 \phi - \cos^2 \theta} = X_{\text{cam1}} \cos \theta + Y_{\text{cam1}} \cos \phi + Z_{\text{cam1}} \sqrt{1 - \cos^2 \phi - \cos^2 \theta} \quad (15)$$

where $(\xi, \phi, \theta) = \text{angles orienting the normal to a candidate plane}$, $\xi = \sqrt{1 - \cos^2 \phi - \cos^2 \theta}$, $Z_p = \text{location on candidate plane of the point } (0, 0, Z_p) \text{ where the optic axis intersects the candidate plane}$.

To obtain the location of the virtual plane which corresponds to the location of the planar patch on the true object, the image coordinates $(X_{\text{img2}}, Y_{\text{img2}})$ for each pixel in the selected subset are converted to sensor coordinates and corrected for lens distortion using (6,7,8,9,10,11). After calculating $(X_{\text{sen1}}, Y_{\text{sen1}}, \text{phd}_1)$, the coordinates $(Y_{\text{cam1}}, Z_{\text{cam1}})$ in the Camera 1 system can be obtained using (7,8) to give

$$\begin{aligned} Y_{\text{cam1}} &= X_{\text{cam1}} \frac{Y_{\text{sen1}}}{X_{\text{sen1}}} , \\ Z_{\text{cam1}} &= \frac{X_{\text{cam1}} \text{phd}_1}{X_{\text{sen1}}} . \end{aligned} \quad (16)$$

Combining (14) and (15), expressions for $X_{\text{cam1}}, Y_{\text{cam1}}$ and Z_{cam1} are obtained in terms of known parameters $X_{\text{sen1}}, Y_{\text{sen1}}, \text{phd}_1$ and the candidate plane's parameters, θ, ϕ and Z_p :

$$X_{\text{cam1}} = \frac{X_{\text{sen1}} Z_p \sqrt{1 - \cos^2 \phi - \cos^2 \theta}}{\text{phd}_1 \sqrt{1 - \cos^2 \phi - \cos^2 \theta} + Y_{\text{sen1}} \cos \phi + X_{\text{sen1}} \cos \theta} ,$$

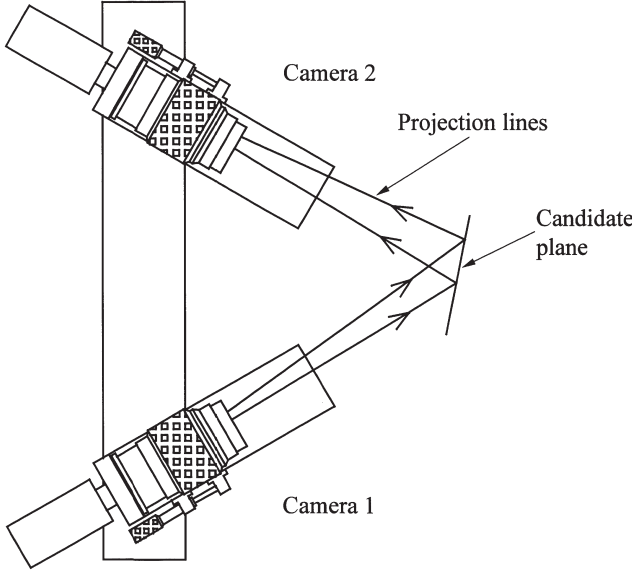


Fig. 8. Schematic representing the projection and back-projection processes used in VIC-3D to determine the orientation and three-dimensional position for subsets

$$\begin{aligned}
 Y_{\text{cam1}} &= \frac{Y_{\text{sen1}} Z_p \sqrt{1 - \cos^2 \phi - \cos^2 \theta}}{\text{phd}_1 \sqrt{1 - \cos^2 \phi - \cos^2 \theta} + Y_{\text{sen1}} \cos \phi + X_{\text{sen1}} \cos \theta} , \\
 Z_{\text{cam1}} &= \frac{\text{phd}_1 Z_p \sqrt{1 - \cos^2 \phi - \cos^2 \theta}}{\text{phd}_1 \sqrt{1 - \cos^2 \phi - \cos^2 \theta} + Y_{\text{sen1}} \cos \phi + X_{\text{sen1}} \cos \theta} . \quad (17)
 \end{aligned}$$

The three-dimensional projected position in the cam1 system of the pixel that has position $(X_{\text{sen1}}, Y_{\text{sen1}})$ is given by (17). Fourthly, the position $(X_{\text{cam1}}, Y_{\text{cam1}}, Z_{\text{cam1}})$ is converted into image coordinates in the cam2 system, $(X_{\text{img2}}, Y_{\text{img2}})$, using (4 – 11) and the known relationship between the cam1 and cam2 coordinate systems. This process, denoted as back-projection, includes a correction for Camera 2 lens distortion. It is worth noting that the process of back-projecting the points to the Camera 2 sensor plane from the candidate plane requires only the position $(X_{\text{cam1}}, Y_{\text{cam1}}, Z_{\text{cam1}})$ and parameters determined by calibration of the two cameras. Finally, the optimal position of the candidate plane is obtained by varying Z_p, θ and ϕ and minimizing a cross-correlation error function, similar to the one used for 2D-correlation, for the subsets of intensity values in both Camera 1 and Camera 2. Initial estimates for Z_p, θ and ϕ , the candidate plane's parameters, are obtained through a graphical user interface. The optimization process uses sub-pixel interpolation to improve the accuracy of the estimated gray levels in Camera 2. A measure of cross-correlation error [58] is employed for the optimization process to reduce the effects of lighting variations between cameras. To obtain

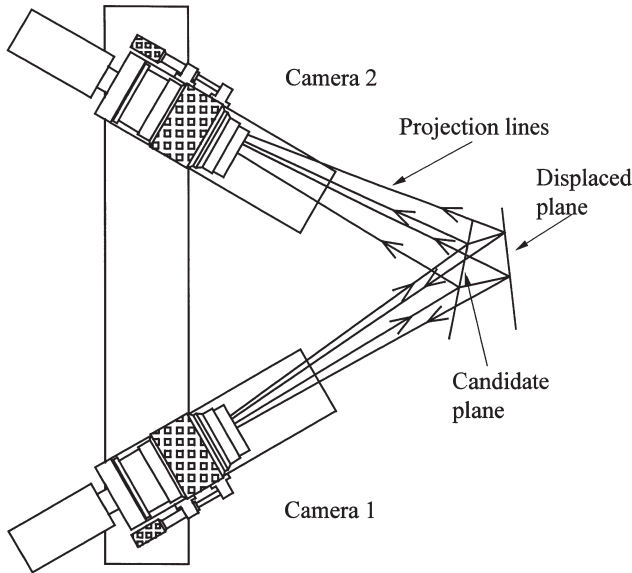


Fig. 9. Projection and back-projection used to determine three-dimensional displacements for subsets

full-field data, initial estimates for the position and orientation of adjoining subsets are the optimal locations obtained for the previous subset.

The process used to obtain three-dimensional surface displacement measurements is shown graphically in Fig. 9. In Fig. 9, the candidate plane is allowed to undergo translations and rotations. Therefore, the points established by the projection of any subset from Camera 1 onto the candidate plane will translate and rotate with the candidate plane. These displaced points are then back-projected into Camera 1 and Camera 2. The gray levels for the projections are compared with the recorded gray levels from images taken by both Camera 1 and Camera 2 after loading the specimen. A cross-correlation error function similar to the one used for profiling is employed to determine the position of the surface point before deformation, as well as translations and rotations at the point.

The error function is similar to those described in Sect. 2.1.2 for two-dimensional correlation. However, for three dimensions, the error function is modified to include intensity data from both cameras. The data includes: (a) a subset from the initial image in Camera 1, (b) a subset from the initial image in Camera 2 obtained by projection of the subset from Camera 1, (c) a subset from Camera 1 at some later time, t_2 , and (d) a subset from Camera 2 at the same time t_2 obtained by projection of the subset from Camera 1. By minimizing the error function for all four images simultaneously, the best-fit candidate plane and its displacements are established. This

process includes perspective distortion directly through the pin-hole camera model used for projection. This is a substantial improvement over previous approaches [55,56,57], which did not include subset distortion due to perspective distortion. It should be noted that the DIC-3D system can handle relatively large in-plane and out-of-plane rotations.

General error estimates for DIC-3D systems are difficult to determine since there are several model parameters that have an effect on the accuracy of the measurements. However, estimates can be provided for a specific range of parameter values. Specifically, the error estimates given below are based on the following parameter ranges; (a) pan angle between cameras in the range 30° to 60° , (b) twist and tilt angles in the range -5° to 5° , (c) distance from camera to object, Z , in the range 0.3 m to 3 m, (d) size of region imaged, D , in the range 10 mm to 0.5 m and (e) $Z/D > 5$ for all experiments.

Results from several experiments performed using model parameters in this range indicate that the error in each component of displacement can be approximated as follows:

- (a) Error in in-plane displacement is of the order of $D/10\,000$, where D is the in-plane dimension of the object that is imaged by the camera,
- (b) Error in out-of-plane displacement is of the order of $Z/50\,000$, where Z is the approximate distance between the sensor plane and the object.

3 Applications

3.1 Two-Dimensional Video Image Correlation

3.1.1 Measurement of Crack-Tip Opening Displacement During Mixed Mode I/II Crack Growths Using DIC-2D

Background. Aging of the commercial aircraft fleet resulting in the increased potential for multi-site damage in the fuselage skin, has heightened the need for methods to predict the residual strength of aircraft components [66,67]. Since stable crack extension occurs in most aircraft fuselage structures prior to collapse, primary emphasis has been placed on deformation-based fracture criteria. Since the fuselage of an aircraft is subjected to various combinations of loading, flaws in the fuselage experience local conditions that include various levels of Mode I, Mode II and/or Mode III behavior; such a state is referred to as mixed mode. Recent studies have shown that a critical Crack-Tip Opening Angle (CTOA) (or equivalently, Crack-Tip Opening Displacement (CTOD) at a specific distance behind the crack-tip) is a viable parameter for predicting crack growth in thin sheet 2024-T3 aluminum under both Mode I [25,26] and Mode II [28,68] loading conditions.

DIC-2D has been used successfully in measuring the in-plane deformations of thin sheet aerospace materials under mixed-mode I/II loading. Specifically,

CTOD, surface displacement and strain field measurements have all been acquired through the use of DIC-2D in laboratory tests [25,28,68]. The subsequent paragraphs will summarize the work done in this area with a detailed explanation of the application of DIC-2D in obtaining CTOD measurements.

Experimental Approach. The test fixture used in this work was a modified Arcan test fixture [28]. The fixture with specimen bolted into place is shown in Fig. 10. The initial value of a/w was 0.17 throughout the tests, where a is the initial crack length and w is the specimen width. Tests were performed for a variety of loading angles, φ , to obtain various levels of K_{II}/K_I in the crack-tip region, where K_I and K_{II} are the Mode I and Mode II stress intensity factors, respectively. The range of K_I and K_{II} values, as well as the second term in the elastic crack-tip solution, are given in [69]. To assess the effect of grain orientation on critical CTOD, specimens were machined in both LT (initial crack perpendicular to rolling direction) and TL (crack parallel to rolling direction) orientations, as shown in Fig. 11.

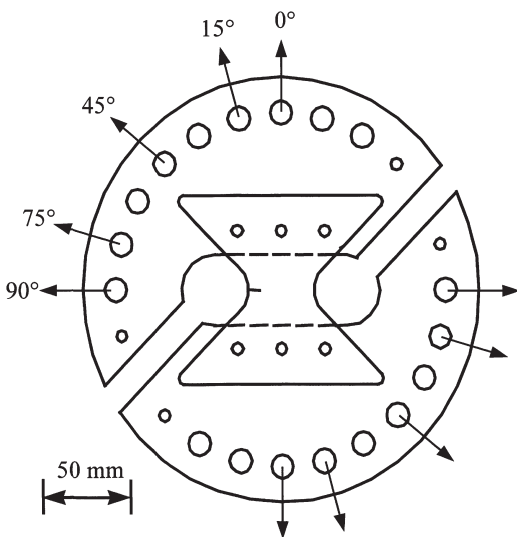


Fig. 10. Arcan test fixture used in mixed-mode I/II tests

During the tests, which involved predominantly in-plane deformations, a single camera system similar to that shown in Fig. 1 was used to record images of the crack-tip region. During the test, in-plane, mixed mode, crack-tip-opening displacement was measured accurately both at initiation and during crack growth using the DIC-2D system, as outlined in [28,68].

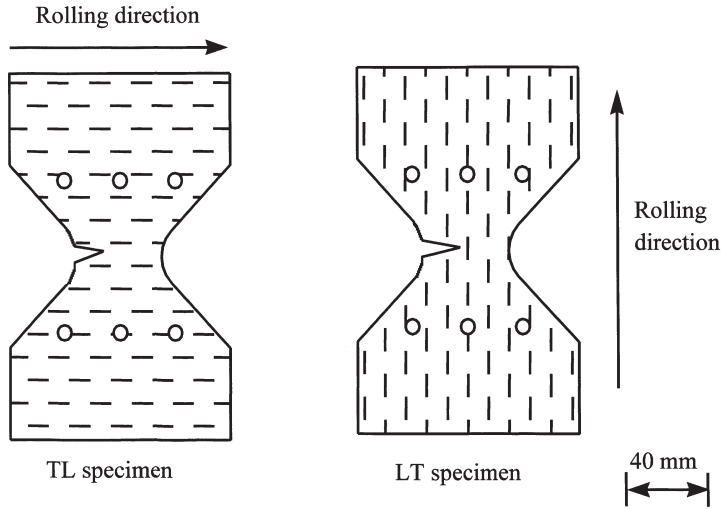


Fig. 11. Arcan test specimens and orientation of crack relative to rolling direction for 2024-T3 aluminum sheet material

Pattern Application. To obtain CTOD at a fixed distance d behind the crack-tip using DIC-2D, the specimen is most-often fatigue pre-cracked to the initial a/w value required for each specimen geometry. Once the initial flaw size is obtained, the specimen is removed from the load-frame and a high contrast, black and white, random pattern is applied to one side of the specimen. Since oversampling is essential for optimum accuracy, each small black region should occupy approximately a 5×5 pixel area. If an area $5 \text{ mm} \times 5 \text{ mm}$ square is imaged by a 512×512 pixel array, each small region should be approximately $49 \mu\text{m}$ in size.

To achieve a usable random pattern of the required size, a thin coating of white enamel spray paint was applied to the surface (white epoxy spray paint was used if the plastic deformation was large and de-bonding of the enamel paint occurred). To apply a high quality black pattern, two methods have been used successfully: (a) a light spray of black paint, and (b) a light coating of Xerox toner powder. When black paint was used as an over-spray, the white paint was allowed to dry and then a fine mist of black paint was applied. Both fine-tipped attachments for airbrushes and spray cans have been used successfully and the method of choice was refined through trial applications. To apply a Xerox toner powder pattern, the surface was lightly spray painted in white. Then, a mist of toner powder was applied to the wet surface until a pattern of sufficient density was observed. Regardless of the method used, the random pattern was evaluated by using the DIC-2D set-up to record an image of the pattern and compute a histogram of the image; optimal patterns have a relatively broad, flat histogram. If the pattern was not satisfactory, it was removed and the surface repainted.

Experimental Image Acquisition. To obtain CTOD during crack growth all experiments were performed in displacement control. The camera was mounted on a two-dimensional translation stage to track the moving crack-tip region and images of the crack-tip region were acquired during crack growth. To minimize the effects of out-of-plane translation during the test, the distance between the camera system and the specimen was maximized. For a distance of 0.60 m to 1 m from the camera to the specimen, a 200 mm lens with a 2× adapter was used to obtain the required magnification.

Prior to initiating the crack-growth test, images of a ruler were acquired to determine the image magnification factor. Typical magnification factors range from 80 to 140 pixels per mm. An image of the crack-tip region, along with two subsets located on opposite sides of the crack approximately 1 mm behind the current crack-tip, is shown in Fig. 12. Images of the crack-tip region were acquired (a) with a small pre-load on the specimen, (b) for load values approximating the value at which crack growth occurs and (c) after a small amount of stable crack growth occurred, where crack growth was less than approximately 1 mm.

Assuming crack growth occurred from left to right, upon completion of crack growth the camera was translated until the current crack tip was located approximately 150 pixels from the left side of the screen. Loading was then increased and images acquired until stable crack growth occurred; the process described above was repeated until sufficient data was obtained or the crack grew outside the imaged area.

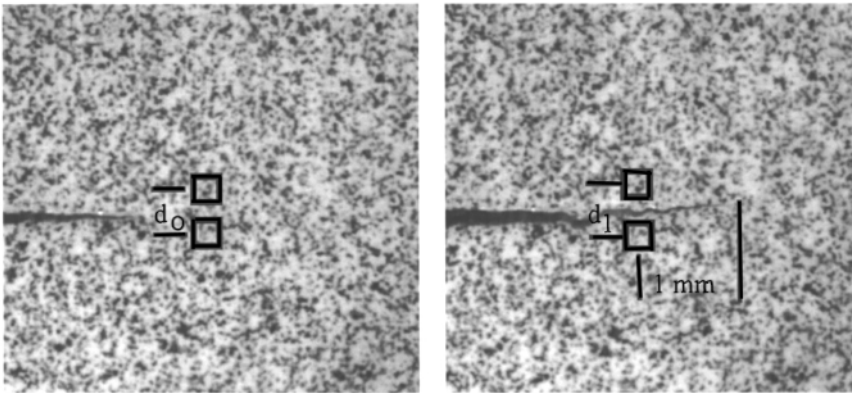


Fig. 12. Location of subsets along crack line for mixed-mode I/II crack-tip opening displacement measurement

Image analysis procedure to obtain CTOD. The measurement of CTOD is shown graphically in Fig. 12, where $CTOD = d_1 - d_0$ at 1mm behind the current crack-tip. To compute the displacements of points located

on either side of the crack line, subsets centered about the points of interest were chosen from the current configuration of the fracture specimen. For most CTOD measurements, subsets ranging in size from 10×10 to 30×30 pixels on both sides of the crack line were used.

Results and Conclusions. As shown in Fig. 13a–c, CTOD for thin rolled 2024-T3 aluminum alloy materials under tension-shear loading varies with grain orientation. Data indicates that critical the CTOD is approximately 20% larger when the crack grows nominally perpendicular to the grain orientation (LT). This observation is consistent with previous experimental results [28,68]. It is worth noting that for shear-type crack growth ($\phi \geq 75^\circ$), the crack surfaces always interfered during crack propagation. Thus, even though the critical CTOD is approximately constant during crack growth, the crack-tip driving force will be reduced for shear-type crack growth, due to frictional losses along the crack line.

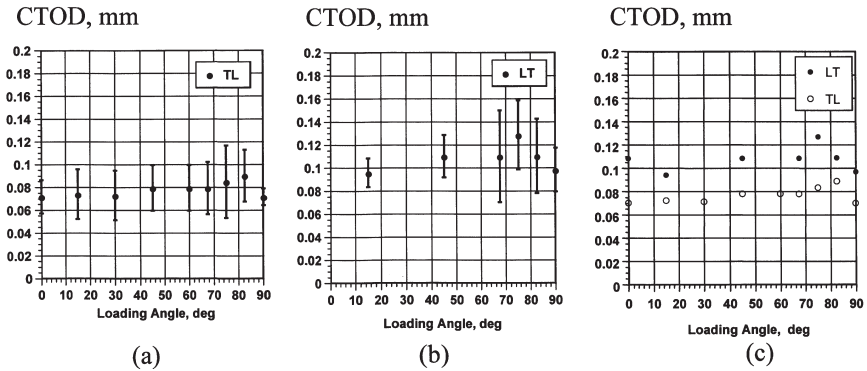


Fig. 13a–c. CTOD results for both TL and LT specimens and all loading angles

Results from mixed-mode I/II loading indicate that (a) the value of critical the CTOD during crack growth approaches a constant after approximately 5 mm of crack extension, (b) the critical CTOD for 2024-T3 is a strong function of the direction of crack growth relative to the rolling direction, with the critical CTOD for cracks growing in nominally the LT direction being 20% larger than for cracks growing nominally in the TL direction.

3.1.2 Local Crack-Tip Closure Measurements Using DIC-2D

Background. The measurement of key quantities in the crack-tip region has been an area of active research for many years. In particular, a simple and effective method for obtaining high accuracy, local measurements of the

crack-opening displacements (COD) in regions 0 to 250 μm behind the crack-tip has been lacking.

A wide range of methods has been developed for measuring COD [70] including clip gages, strain gages and interferometric methods. Clip gages are easy to use, but they only provide information at positions that are remote from the crack-tip location. Thus, these measurements provide little information about the current closure conditions at the crack-tip. Strain gages applied to various locations near the crack-tip, including back-face and side-face positions, have been used to characterize closure loads. However, these methods provide data at a fixed position on the specimen, which means that the data cannot be obtained at pre-specified distances behind the growing crack-tip. Interferometric methods include moiré interferometry [71] and the indentation method [70]. Moiré methods are quite accurate and can be used to quantify COD along the crack line. However, the application of a grid to the polished surface remains a drawback of the method. The indentation method has been used successfully to measure COD in a wide range of applications, including elevated temperature crack growth. As with other methods, the position of the indentations is fixed on the specimen, providing data at positions that vary in distance behind the crack-tip.

New Approach to COD Measurement. To simplify the process of obtaining COD at arbitrary distances behind the moving crack-tip, a vision-based methodology has been employed. The set-up consists of a far-field microscope, three-dimensional translation stage, a camera-digitizing board-PC combination for recording and storing images of the region and the DIC2-D software for obtaining the relative displacements of points on either side of the crack line.

Using a far-field microscope lens, the system is capable of imaging areas 0.8 mm \times 0.8 mm or smaller. The specimen surface was polished to obtain maximum contrast. By applying a dark, random pattern to the polished surface and illuminating the surface using an on-axis light source, the polished region appears much lighter than the dark pattern, providing a high contrast, random intensity variation for later analysis using the DIC2-D software.

Two methods were developed to obtain a high-contrast intensity pattern of the appropriate density on the polished surface. First, a modification of the method used for applying Xerox toner powder in Mode I/II testing was used. In this case the toner powder was filtered, using 11 μm filter paper and a compressed air source, to obtain only the smaller particles for application to the surface. By applying the filtered powder onto the polished surface and heating it for a few minutes to 100 $^{\circ}\text{C}$, the toner powder bonds to the surface. A typical pattern obtained this way is shown in Fig. 14. Average size of the random pattern was $\approx 20 \mu\text{m}$ after heating.

Since the pattern developed this way is suitable for tests in air, it was used to obtain all the results for this work. However, to obtain a smaller,

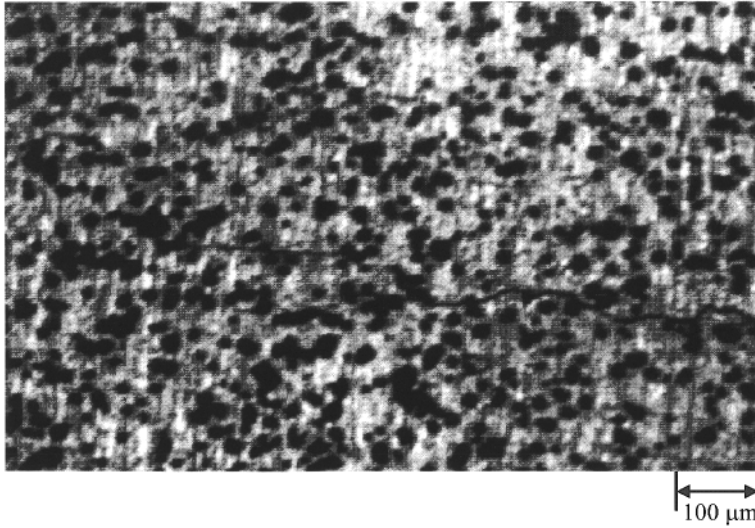


Fig. 14. Pattern obtained using filtered xerox toner powder for crack closure measurements at high magnification

more durable pattern for use in vacuum or corrosive environments, a mask was made using electron-beam lithography. The mask is manufactured only once and then used each time a new experiment is to be performed. A typical pattern obtained using a lithographic mask is shown in Fig. 15. The pattern shown in Fig. 15 was produced using the following process. Firstly, the polished specimen's surface was spin-coated with photoresist. Secondly, a lithographic mask with $8\text{ }\mu\text{m}$ features was placed on the coated surface and an ultraviolet light source was used for illumination. Thirdly, the exposed portions of the photoresist pattern were removed through a development process. Fourthly, a thin layer of tantalum was evaporated onto the specimen surface. Fifthly, the remaining photoresist was removed through a final development process, leaving a tantalum pattern on the polished surface. Since any type of pattern can be obtained by electron-beam lithography, much smaller patterns can be placed on the specimen for use at higher magnification.

System Accuracy. A simple tension test was performed using a dog-bone specimen made of 2024-T3 aluminum. By measuring the relative displacements along the direction of loading for three 91×91 pixel subsets in a 0.5 mm by 0.30 mm area that were separated by 0.16 mm , the value for strain along the line was determined to have a standard deviation of $200\text{ }\mu\text{strain}$. Thus, an estimate for the displacement error in the method is approximately 30 nm or 0.05 pixels at the magnification used in this work.

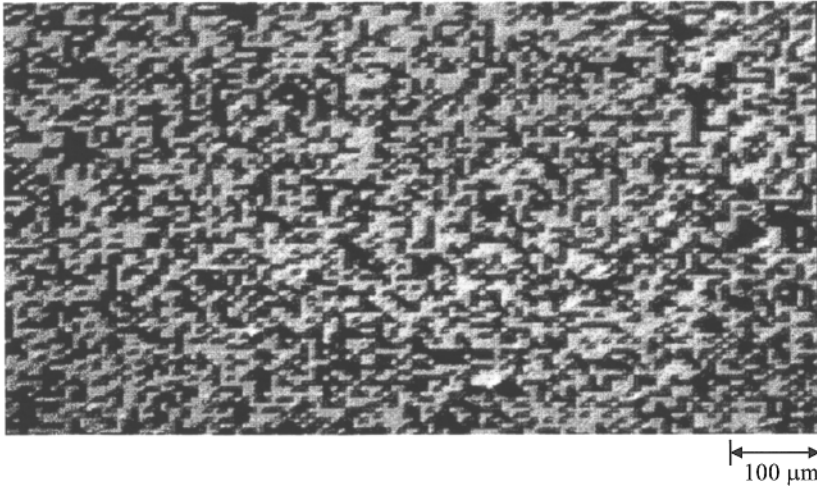


Fig. 15. Typical pattern obtained using a lithographic mask for crack closure measurements at high magnification

Crack Closure Measurements. Figure 16 presents the measurement of crack-opening displacement as a function of cyclic load at distances of 0.075 mm and 0.224 mm behind the current crack-tip. The specimen was machined into an extended compact tension geometry from aluminum alloy 8009, with width of 38.1 mm, thickness of 2.3 mm and $a/w = 0.54$. During the test, $\Delta K = 4.4 \text{ MPa m}^{\frac{1}{2}}$ and the R-ratio was held constant at 0.10.

As shown in the measured COD curves for two locations behind the crack-tip, a clearly defined change in slope was observed, corresponding to the elimination of crack surface contact at each position behind the crack-tip [72,73]. Furthermore, the data shows that the load at which crack surface contact was eliminated at the free surface of the specimen is a function of position behind the crack-tip.

3.1.3 Large Specimen Tests

Background. In recent years, new materials have been developed for use in a wide range of applications: functionally gradient materials for advanced applications in the transportation and defense industries, toughened ceramics for defense applications, and advanced composite materials for aerospace uses. In many cases, the development of new materials is driven by the conflicting demands of simplicity in manufacturability, adequate strength and reduced weight.

Recently, after receiving congressional approval to build the Space Station, NASA has embarked upon a program to reduce the weight of the Space

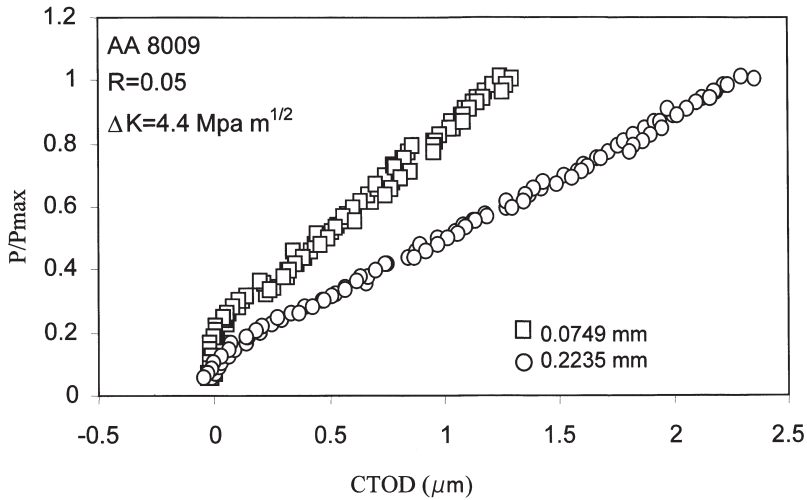


Fig. 16. Measured crack-opening displacement as a function of cyclic load at two locations behind the current crack-tip

Shuttle so that additional Space Station components can be transported into space. In particular, NASA proposed to manufacture the external tanks of the Space Shuttle using AL-2195, an aluminum-lithium alloy, that would reduce weight by 33.4 kN.

To demonstrate that the proposed alloy had the required structural properties, NASA initiated an extensive test program. Results from early biaxial tests indicated that there was a soft spot in the center of the manufactured cruciform specimen. After several metallurgical studies were completed, it was conjectured that the soft spot was due to a combination of residual stresses in the material and the machining techniques used to make the specimen. To understand better how the machining processes affected the local material response, the full-field deformations throughout the center portion of the test section were measured during loading and unloading of the specimen. In the following sections, the results from using a DIC-2D system to measure the full-field deformations in a critical region of an AL-2195 test specimen are presented.

Experimental Set-up. The test specimen is shown in Fig. 17. The cruciform test specimen, which has four grip regions, was machined for use in a biaxial test frame. For this work, the specimen was uniaxially loaded in a 0.448 mN test frame, using one set of grips. The center region of the cruciform specimen was milled to a depth of 3 mm on both sides to obtain a central, square, recessed test section that was 6.4 mm thick.

During the tests, a DIC-2D system similar to the one shown in Fig. 1 was used to record images. Even though the specimen was expected to undergo

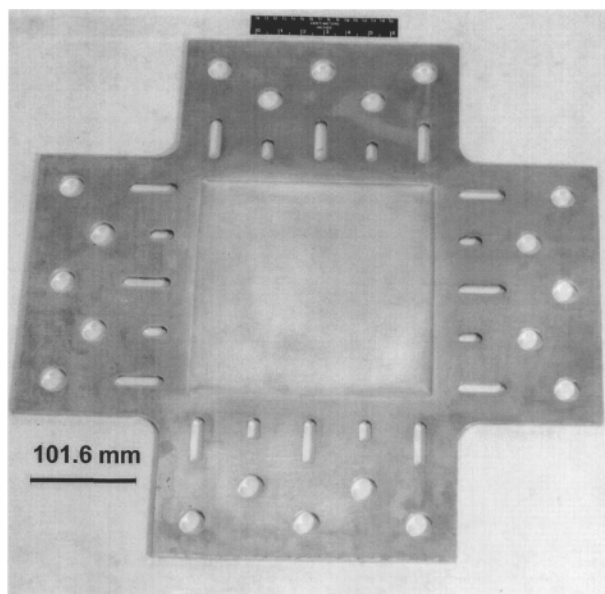


Fig. 17. Cruciform specimen machined from Al-2195

predominantly in-plane deformation, the DIC-2D system was placed 2 m from the test specimen to minimize the effects of any out-of-plane motion on the measured displacements. To increase mobility and adaptability in the test facility, the digital camera was mounted on a heavy, professional Bogen tripod during the test. To stabilize the lens system, a lens support mount was machined and used during the test.

Due to concerns about the center region of the test specimen, the region imaged was reduced to 46 mm by 43 mm; based on strain gage data from previous tests, this region appeared to have large gradients in strain. A Canon 200 mm lens was used for imaging the central region.

Prior to loading the specimen, and after the optical set-up was complete, images of a ruler mounted to the surface of the specimen were acquired. Using these images, the magnification factor was approximately 11.5 pixels per mm. After acquiring ruler images, the central region was lightly spray painted with white and black paint to obtain a high-contrast random pattern.

All experiments were performed under displacement control. The loading process was as follows: (a) the load was increased incrementally to a maximum of 320.3 kN, (b) the load was decreased incrementally until fully unloaded, and (c) the load was increased incrementally to the maximum load. Images were acquired every 4.448 kN throughout the loading-unloading-reloading process.

To obtain the strain field, $\varepsilon_{yy}(x, y)$, along the loading direction, the in-plane displacement field was determined using the DIC-2D algorithm. Data

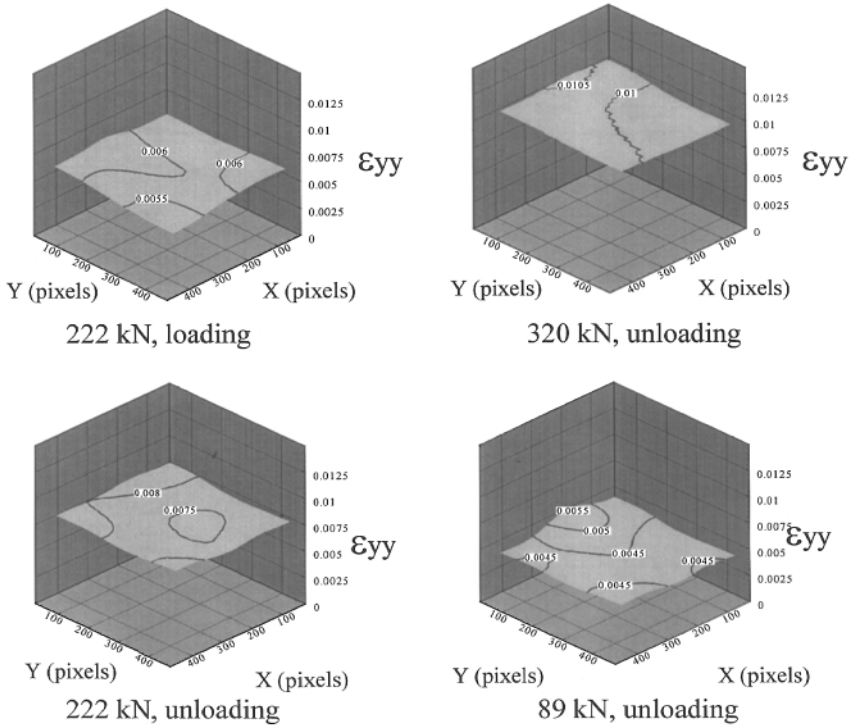


Fig. 18. Measured ε_{yy} strain field in center region of cruciform specimen during uniaxial tensile loading and unloading

was acquired for the central 400×400 pixel region of the image. The displacement field was obtained at 1681 locations using 21×21 pixel subsets (overlapped by 10 pixels) on a 41×41 grid in each image. After computing the 2D displacement field at each point, the vertical displacement field was fitted with a smoothed surface using the procedures described previously [5,7]. The resulting ε_{yy} field at four different loads (two ε_{yy} fields during initial loading and two ε_{yy} fields during unloading) is shown in Fig. 18. Table 2 presents both the average strain value over the field, $\varepsilon_{yy}^{\text{avg}}$, and the standard deviation in the strain for all loading.

Discussion of Results. The data in Fig. 18 for the strain field $\varepsilon_{yy}(x, y)$ indicates that the strain gradients were negligible over the center region. Furthermore, the data clearly showed that the deviations in strain throughout the loading-unloading-reloading processing were small. Thus, the results did not indicate the presence of a soft spot in the material, demonstrating that the material did not exhibit unwanted, localized deformations due to either residual stresses or machining.

After discussions with NASA personnel, it was concluded that the strain gage data from this test, and previous tests, was suspect due to a combination of wire mislabeling and gage malfunctioning. Thus, the DIC-2D data provided a high degree of confidence that AL-2195 could be used for Space Shuttle applications.

3.2 Three-Dimensional Video Image Correlation

3.2.1 Profiling of Structures for Reverse Engineering

Background. Reverse engineering of components has become increasingly important to many government agencies, particularly since the downsizing of federal government has led to the loss of established contractors and associated component documentation. To address this concern, a wide range of methods has been developed for accurately measuring the shape of a part. The techniques include contacting methods (e.g. precision coordinate-measurement machines) as well as non-contacting methods (e.g. optical systems, computer-aided tomographic systems, and sonar-based systems).

The goal of each measurement system is to accurately measure the shape of an object as rapidly as possible. In the following sections, the procedure described in Sect. 2.2.5 is used to accurately measure the shape of an object. To increase the accuracy of each measurement, several partially overlapping regions of the object are measured. To obtain a single representation for the object, advanced data processing algorithms are used to combine the measurements.

Experimental Set-up. The three-dimensional measurement system used in this work is similar to the one shown in Fig. 5 and Fig. 6. The cameras were Pulnix digital cameras with Bitflow Raptor digital data acquisition boards. Canon 100 mm F4 macro lenses were used for imaging the object. A custom camera mount was developed [58] that served as an adapter from the C-mount to the Canon FD mount, as well as the main support for the lens and camera. Both cameras were mounted on Newport translation stages having a least count accuracy of $0.10\text{ }\mu\text{m}$. The camera-translation-stage combinations were firmly mounted on an extruded aluminum bar, which provided maximum rigidity and reduced relative motion between the two cameras. Calibration was performed using a $10\text{ mm} \times 10\text{ mm}$ grid divided into 100 squares, with point-to-point accuracy of the grid being $\pm 4\text{ }\mu\text{m}$. The grid was oriented at $\approx 45^\circ$ from the row direction during the calibration process, which gives the best accuracy in locating the grid intersection points with the current algorithm. To enhance contrast during calibration the grid was mounted on a translucent plate and illuminated from the rear. The accuracy of the set-up (as indicated by the calibration process) was $\pm 4\text{ }\mu\text{m}$, which is consistent with the reported accuracy of the calibration grid.

To obtain a random pattern of appropriate size for use in imaging portions of a 12 mm area, Xerox toner powder and white paint were used. The procedure used was the same as outlined in Sect. 3.1.1.

For this work, a twenty-five cent coin was used as the object; feature heights were less than 0.200 mm across the coin. To obtain maximum accuracy in the measurements, several overlapping images of the object were obtained at high magnification. To achieve this goal, the object was moved three times, resulting in four overlapping data sets.

Registration of surface patches. Multiple patches are often required when profiling objects due to (a) partial occlusion of the object surface, (b) limited field of view for the experimental set-up, or (c) requirements for increased resolution for measurements. Any combination of these factors will make it impossible to profile the entire surface using one pair of images. For the object used in this experiment, a twenty-five cent coin, multiple patches were used to improve the accuracy of the final surface profile, which consisted of a set of (X, Y, Z) coordinates. Figure 19 shows the four patches of data obtained from the profiling system used in this experiment. Each patch consists of 5040 data points obtained by correlating overlapping 21×21 pixel subsets from the images. To obtain adjacent patches, the object was translated and rotated so that the new set of images had approximately 20% overlap with the previous set of images. Based on the calibration error estimates, the accuracy of the profile measurements for this set-up is estimated to be $\pm 4 \mu\text{m}$ for each patch.

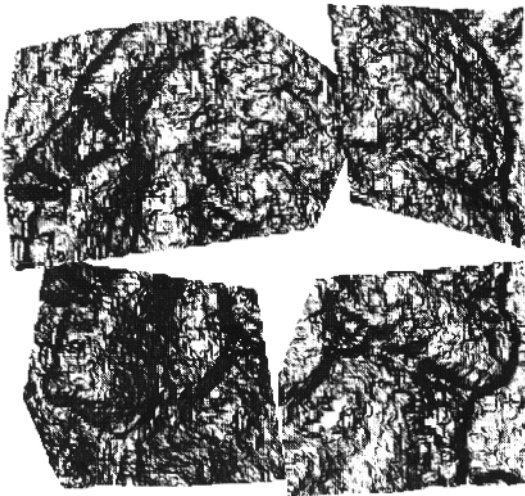


Fig. 19. Measured three-dimensional positions for four overlapping regions of an object

Ideally, the object or camera movement before acquiring a new set of images would be accurately quantified to simplify the registration process. Unfortunately, extremely high accuracy in the object or camera motion would require expensive equipment and an elaborate experimental set-up. In this work, an automatic surface registration algorithm was developed which does not require high accuracy motion data for the object or camera. In fact, the algorithm only requires approximate overlapped positioning of surface patches as initial guesses. Estimated relative position (initial guess) among surface patches can be obtained either from the measurement process (e.g., data from a robot-arm control-system used to move the object or camera system) or by operator interaction. In the latter case, the operator identifies geometric features on the surface patches and drags them across the computer graphic screen to obtain approximate alignment of the patches. Figure 20 shows the positions of the four patches in Fig. 19 after using crude initial guesses for the object motion to begin the registration process.



Fig. 20. Initial estimate of translations and rotations for the recombination of regions

After applying the initial guesses, each of the surface patches is represented by a triangularized mesh generated from the measured data sets. The triangularized meshes for the various patches must overlap so that the algorithm can compare geometric shapes in the overlapped area and find the best match. The algorithm is responsible for accurately determining the true rigid body transformation between surface patches so that they can be registered to form a complete model of the object surface.

The registration algorithm developed for this work detects overlapped areas among surface patches and creates pseudo-corresponding point pairs

along the surface normal in the overlapped area. Then, an optimization process is performed to minimize the distance between pseudo-corresponding point pairs by varying the rigid body transformation parameters for three of the surface patches. Final positions are achieved by iteratively updating the position of the surface patches and corresponding point pairs. It should be noted that the algorithm also attempts to reduce registration errors that may be produced by the order in which the patches were registered. Eventually, the algorithm allows all patches to adjust their final position to minimize gaps due to accumulated registration errors between patches.

After completion of the registration, overlapped surface patches undergo mesh topology operations so that they are merged together to generate a single, consistent polygon representation of the object surface. Figure 21 shows the final object profile, obtained by reconstruction of the surface patches.

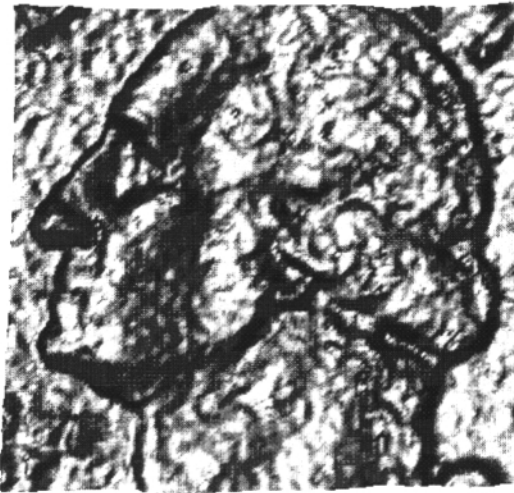


Fig. 21. Representation of the final positions of data points after optimal recombination of four overlapping regions

Summary. Three-dimensional image correlation algorithms can be used to obtain surface profile data with high accuracy. By combining the power of advanced data processing techniques with DIC-3D measurement methods, it is now possible to obtain full, 360° surface representations for complex objects. The geometric models obtained from this approach can be used to create CNC code for precision manufacturing of mechanical parts, thereby facilitating the process of reverse engineering.

3.2.2 Measurement of Three-Dimensional Surface Deformations in Wide Panels Using DIC-3D

Background. As the current fleet of commercial, military, and private aircraft continues to age, and with many aircraft exceeding their original design life, techniques are being developed to aid in the evaluation of aircraft structures and materials. As noted in earlier sections, two-dimensional digital image correlation has been used for many years to accurately measure the in-plane displacements of planar structures under a variety of loads. Because aircraft components and typical aerospace laboratory test specimens deform in a complex manner when loaded, surface measurement systems must be able to make accurate measurements in three-dimensional space. For example, for wide, thin panels fabricated from 2024-T3 aluminum and subjected to tensile loading, the presence of a flaw in the structure will cause the panel to buckle out-of-plane during crack growth. For this case, the DIC-3D system described in Sect. 2.2 is required for accurate determination of the full-field, three-dimensional displacements during deformation. In the following sections, results obtained using the DIC-3D system for measurement of 3-D displacements during tensile loading of center-cracked fiber-reinforced composite and 2024-T3 aluminum panels will be presented.

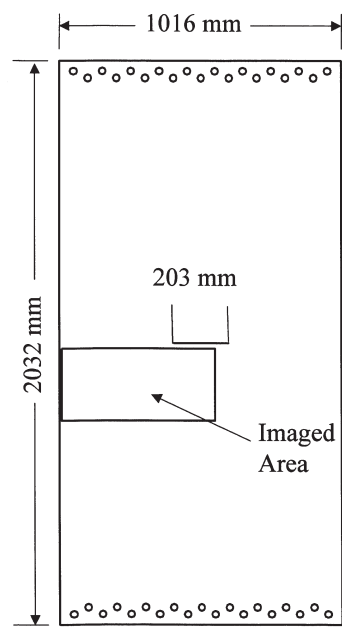


Fig. 22. Wide panel geometry for the 2024-T3 aluminum panel

Test Specimen and Testing Procedure. All tests were performed at NASA Langley Research Center in Hampton, Virginia; the aluminum panels were tension tested in a 1.34 MN tension test frame within the Mechanics of Materials Branch and the fiber-reinforced composite panels were compression tested in a similar test frame in the Structural Mechanics Branch.

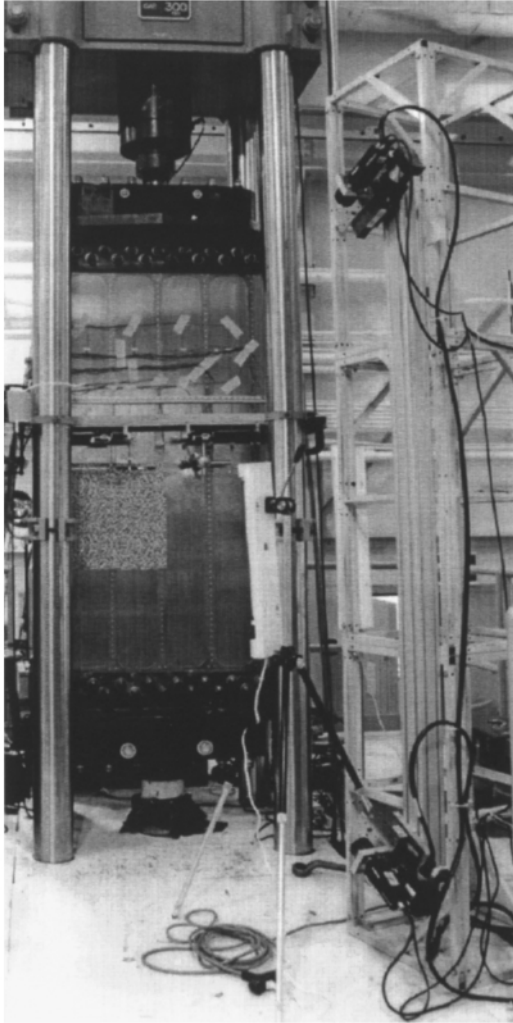


Fig. 23. Photograph of wide panel specimen and imaging set-up in 1.34 MN test frame

The wide panel geometry for the 2024-T3 aluminum panel is shown in Fig. 22 and a photograph of a wide panel specimen with high contrast pattern already applied is shown in Fig. 23. The area imaged on the aluminum sheet is approximately 500 mm wide by 260 mm tall and is located just below the center crack, extending from one edge of the sheet past the centerline of the specimen. All tests were performed under displacement control. Images were acquired every 8.9 kN until crack growth occurred. After initial crack growth, images were acquired at intervals of approximately 4 mm of crack growth until final fracture.

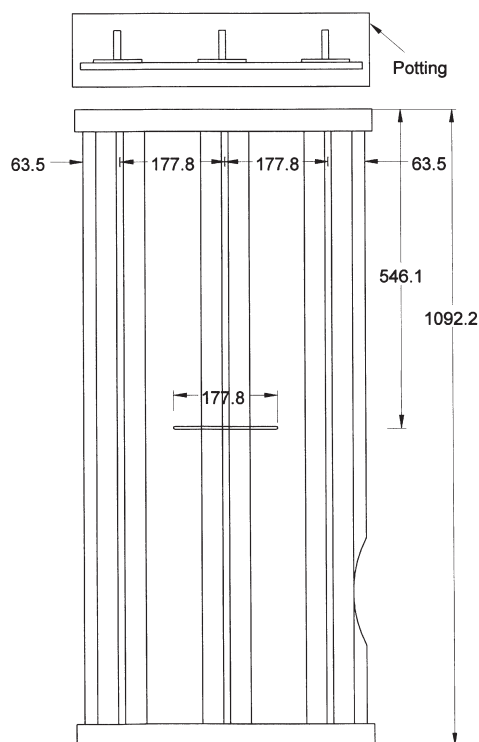


Fig. 24. Geometry for integrally-stiffened composite panel with end potting for distribution of compression loading

Compression testing was performed on a composite reconstruction of a stub box upper wing cover panel. The geometry for the integrally-stiffened composite panel is shown in Fig. 24. The composite panel was 1.09 m long, 0.482 m wide, nominally 12 mm thick and made of Kevlar-stitched, resin-film-infused, graphite-epoxy. Stiffening was provided by integral T-sections on the back of the composite panel. The panel was potted in 38.1 mm thick concrete on each end to improve the uniformity of compressive load distribution. A

flaw was introduced into the panel by cutting a 2.38 mm radius notch through the panel and stiffener in the center region. Since strain gages covered most of the skin side of the panel, the pattern was applied around the gages and lead wires, as shown in Fig. 25.

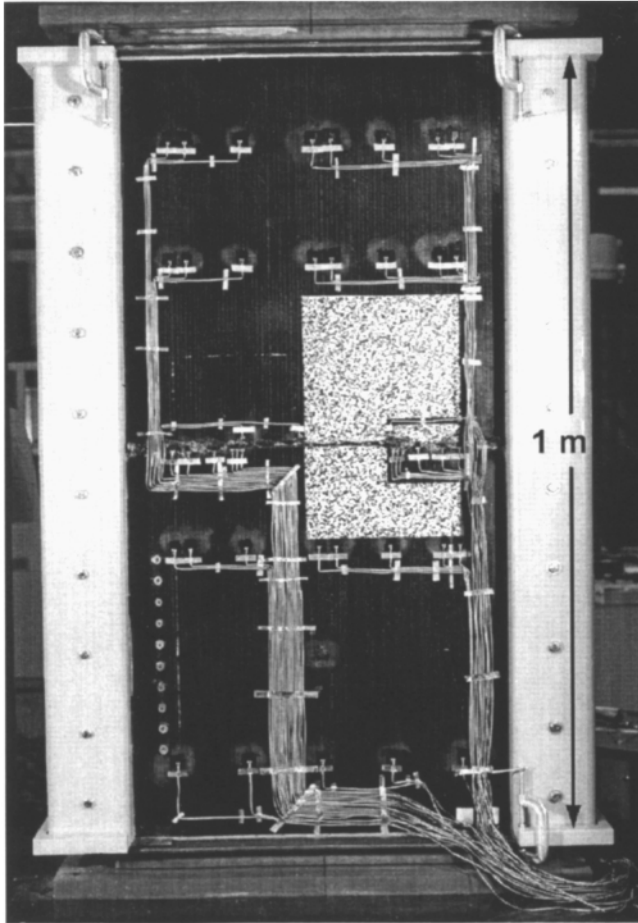


Fig. 25. Photograph of composite panel with applied 3M vinyl pattern, strain gages and knife edges to prevent wrinkling on edges

Image Acquisition System for Large Area Interrogation. Due to the physical size of the region to be imaged for both panels, several modifications were required so that a DIC-3D system could be adapted for this work. First, to improve the accuracy of the measured three-dimensional displacement components, the camera-translation-rotation stage combinations

were mounted near opposite ends of a 2 m long, extruded aluminum bar. The bar was then mounted vertically to a 2 m by 0.7 m by 0.7 m modular frame structure. Secondly, smaller focal length 28 mm Nikon lenses were used for imaging of the large areas. Thirdly, due to the inaccessibility of the camera-translation-rotation stage units, computer-controlled translation stages accurate to $\pm 0.10 \mu\text{m}$ were used to move the cameras for the calibration process. Fourthly, to simplify the process of obtaining a high-contrast random pattern for large areas, a pattern was electrostatically printed onto a 3M adhesive-backed vinyl material. The vinyl material was then temporarily placed in the region of interest for alignment and then firmly pressed onto the surface to release micro-encapsulated epoxy for a more permanent application. Fifthly, a range of lighting methods employed successfully, including halogen flood lights, fluorescent lamps, fiber-optic bundles and incandescent light sources. In each case, the primary goal was to obtain an even distribution of lighting throughout the area of interest.

Calibration of the modified DIC-3D system followed the procedure outlined in Sect. 2.2.2-2.2.4. Due to the size of the experimental set-up, all experimental equipment was placed in its final position and calibrated using a 0.4 m square calibration grid placed against the surface of the test specimen. After calibration, the grid was removed and testing was begun.

All images were analyzed using DIC-3D software which implements the procedure described in Sect. 2.2.5. The software computes the three-dimensional positions and displacements for a field of points for each load level of interest.

Wide Panel Results: Tension of Center-cracked Aluminum Panel.

The load-crack extension curve for the 2024-T3 aluminum sheet is shown in Fig. 26. As can be seen in the Fig. 26, crack growth began at 150 kN, continued in a stable manner up through the maximum load of 269 kN until unstable crack growth fractured the panel at a load of 241 kN.

Figure 27 presents contour plots for all three components of displacement for a load of 240.2 kN just before final fracture. Figure 28 presents the out-of-plane displacement for a horizontal line $Y = -25 \text{ mm}$, below the crack line in Fig. 22. As shown in Fig. 28, the buckling of the panel continued to increase as the crack grew, reaching a maximum of 25 mm just before failure. Furthermore, inspection of Fig. 27 and 28 indicates that the edge of the panel appears to be flat during loading, with the centerline region showing increased buckling. This observation suggests that load transfer into the remaining ligament for a center-cracked sheet will tend to flatten these areas.

Wide Panel Results: Compression of Center-notched Composite Panel. For the composite panel shown in Fig. 25, full-field contours for all three displacement components at the maximum load of 1.34 mN are shown

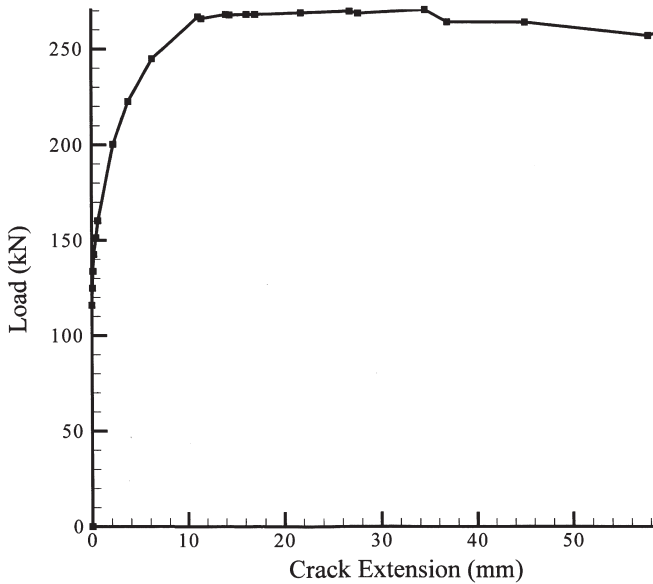


Fig. 26. Load-crack extension data for 2024-T3 aluminum wide panel test

in Fig. 29, 30, and 31, respectively. The maximum measured displacement in the U , V and W fields were $U_{max} = 0.701$ mm, $V_{max} = -3.56$ mm and $W_{max} = 2.77$ mm, respectively.

The DIC-3D data for the out-of-plane displacement was compared to DCDDT measurements from a single point on the panel. The DCDDT was located on the web of the central stiffener on the back of the panel, approximately 46 mm above the notch centerline. The DIC-3D measurements were obtained at the same vertical and horizontal position on the opposite side of the panel. Figure 32 presents a comparison of the results. It can be seen from this comparison that the data agree quite well. The initial movement of the specimen can be seen in the data, as well as the linear variation in the out-of-plane displacement after initial straightening occurred. The difference between the image correlation data and the DCDDT data near the maximum displacement position can be explained by the fact that the positions monitored by the two methods are not exactly the same. The DCDDT tracks a point in space, while the image correlation technique tracks a point on the specimen surface. Thus, as the panel is compressed to a greater degree, these two points become farther apart, resulting in a small difference in the measurements.

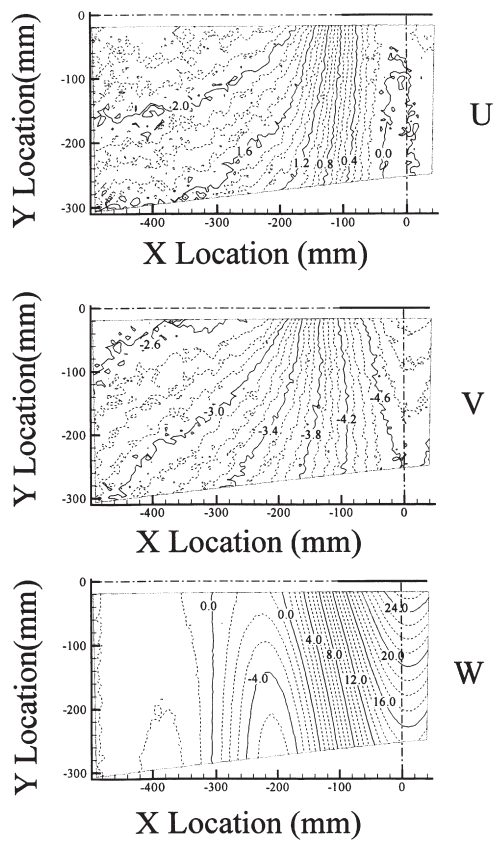


Fig. 27. Contour plots for all three components of displacement for tensile loading of 2024-T3 wide panel just prior to final fracture

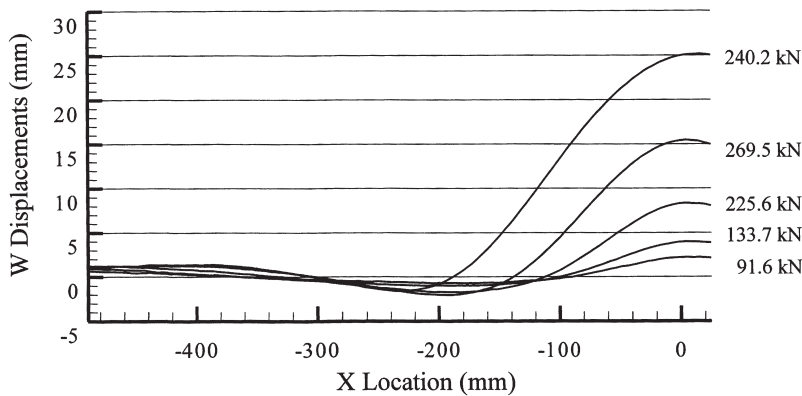


Fig. 28. Out-of-plane displacement as a function of loading along a horizontal line $Y = -25$ mm below the crack line in 2024-T3 wide panel test

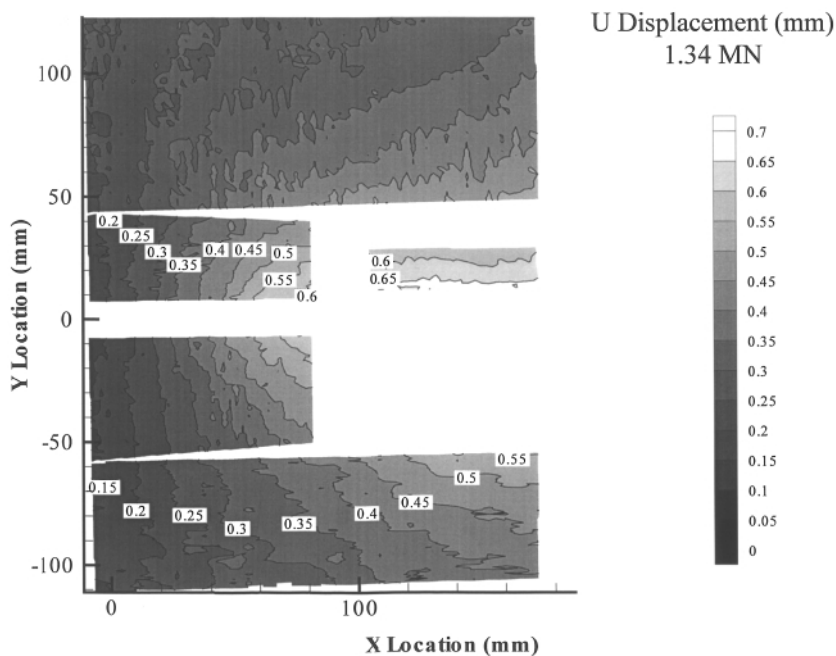


Fig. 29. *U*-Displacement field for composite panel at maximum load

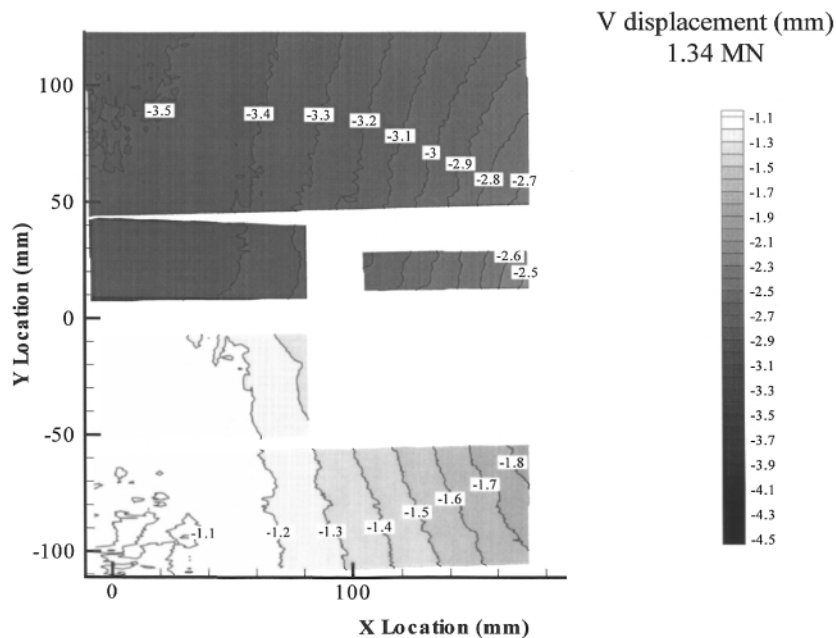


Fig. 30. *V*-Displacement field for composite panel at maximum load

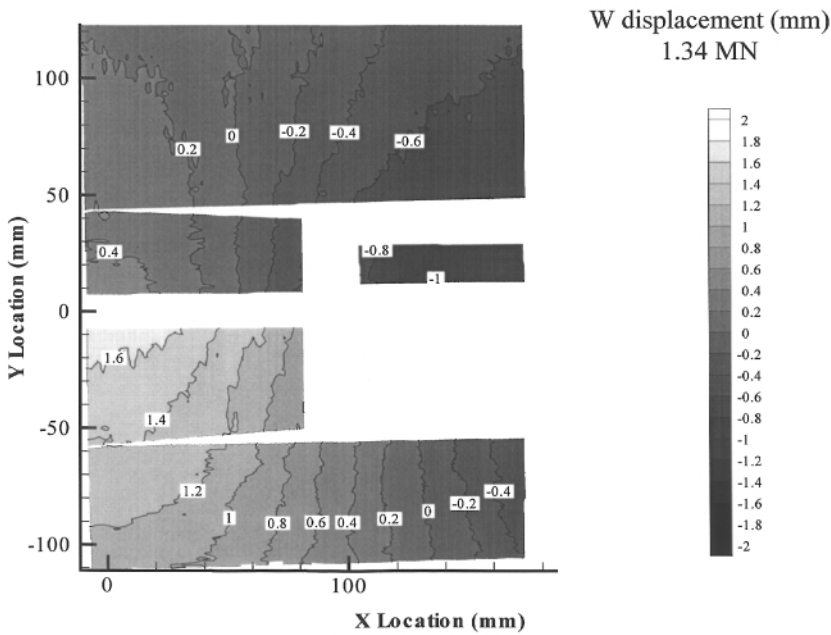


Fig. 31. W-Displacement field for composite panel at maximum load

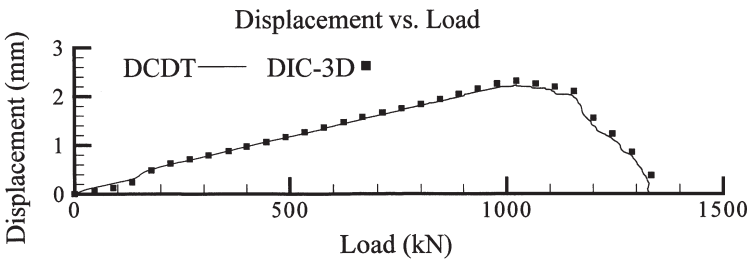


Fig. 32. Comparison of DCDT and W-Displacement measurements at one position for all loads

4 Discussion

With regard to the DIC-2D and DIC-3D methods, a synopsis of the advantages and disadvantages are provided in the following paragraphs. First, the advantages of the DIC-2D method are (a) simplicity of system calibration, (b) ease in applying random pattern (vinyl pre-manufactured pattern, light spray paint) for displacement and strain measurements, (c) user-friendly software and imaging system for real-world applications, (d) well-defined displacement error estimates for current DIC-2D systems (± 0.02 pixels), and (e) ability to use the system for both large and small areas. The primary

disadvantages of any two-dimensional imaging and measurement system are (a) the out-of-plane displacements relative to the camera must be minimized to ensure that the measured displacements are accurate and (b) the object should “approximate” a planar surface both before and after deformation.

With regard to the DIC-3D method, the advantages are (a) ability to make measurements on both curved and planar surfaces, (b) ability to measure both surface profiles and full-field, three-dimensional surface displacements, (c) availability of user-friendly software to simplify the process of acquiring and analyzing images, (d) potential of method in field applications for both large and small structural measurements, and (e) fully digital recording platform, which provides potential for real-time measurements as computer technology advances. Disadvantages of the current method are (a) expense of the equipment required for a fully-integrated system and (b) need for precision calibration grids (or precision, long-travel, three-dimensional translation stages) to calibrate the DIC-3D system over a range that spans the size of the object to be studied.

With regard to commercial level digital image correlation software, several programs have appeared on the market to meet the need of those who wish to use image correlation without having to develop their own software. The availability of such software eliminates the time-consuming task of developing and validating user-friendly algorithms that can acquire and analyze images to obtain displacements and strains for components under load.

5 Summary

Computer vision methods have been successfully developed and applied to the solution of a wide range of scientific and engineering problems, including diverse areas such as fracture mechanics, bio-mechanics, constitutive property measurements in complex materials, model verification for large flawed structures and non-destructive evaluation. Two-dimensional computer vision has been applied successfully to study the deformations of planar regions ranging in size from 0.5 mm to 1 m, in environments that include water, high-temperature air and standard laboratory conditions. Three-dimensional computer vision was used to accurately measure the deformations of curved and planar structures ranging in size from 4 mm to 1.3 m in both field and laboratory conditions.

Applications currently being pursued include (a) use of specially designed cameras for simultaneous measurement of surface deformations and temperature, (b) development of new methods for calibration of multiple camera systems to simplify the process of measuring accurate surface deformations on very large structures, and (c) adaptation of the two-dimensional method for use in measuring surface profiles from multiple scanning electron microscope images.

From our perspective, the last sixteen years have shown conclusively that both the DIC2-D and DIC3-D systems are robust, accurate and relatively simple to use in most applications. Thus, the range of applications for which the methods can be applied successfully seems to be growing rapidly as scientists and engineers use the method and begin to understand the true capabilities of the DIC2-D and DIC3-D systems.

Acknowledgements

The authors wish to thank Mr Michael Boone, Mr Hubert Schreier, Mr Glen Hanna, Dr David S. Dawicke, Dr Wei Zhao and Dr Audrey Zink for their assistance in completing this manuscript. In addition, the support of Dr Charles E. Harris and Dr James C. Newman, Jr in the Mechanics and Materials Branch at NASA Langley Research Center is deeply appreciated. Through their unwavering technical and financial assistance, the potential of the DIC-3D method is now being realized. Finally, the support of Dr Pramod Rastogi throughout the development process is gratefully acknowledged.

References

1. W. H. Peters, W. F. Ranson: Digital Imaging Techniques in Experimental Stress Analysis, *Opt. Eng.* **21**, 427 (1981) [323](#), [324](#)
2. M. A. Sutton, W. J. Wolters, W. H. Peters, W. F. Ranson, S. R. McNeill: Determination of Displacements Using an Improved Digital Correlation Method *Image Vis. Comput.* **1**, 133 (1983) [324](#), [331](#), [331](#)
3. M. A. Sutton, S. R. McNeill, J. Jang, M. Babai: The Effects of Subpixel Image Restoration on Digital Correlation Error Estimates, *Opt. Eng.* **27**, 173 (1988) [324](#), [324](#), [331](#), [331](#)
4. M. A. Sutton, M. Cheng, S. R. McNeill, Y. J. Chao, W. H. Peters: Application of an Optimized Digital Correlation Method to Planar Deformation Analysis, *Image Vis. Comput.* **4**, 143 (1988) [324](#), [324](#), [331](#), [331](#)
5. M. A. Sutton, H. A. Bruck, S. R. McNeill: Determination of Deformations Using Digital Correlation with the Newton-Raphson Method for Partial Differential Corrections, *Exp. Mech.* **29**, 261 (1989) [324](#), [324](#), [331](#), [331](#), [353](#)
6. M. A. Sutton, H. A. Bruck, T. L. Chae, J. L. Turner: Development of a Computer Vision Methodology for the Analysis of Surface Deformations in Magnified Images, ASTM STP-1094 on MICON-90, Advances in Video Technology for Microstructural Evaluation of Materials, 109 (1990) [324](#)
7. M. A. Sutton, J. L. Turner, T. L. Chae, H. A. Bruck: Full Field Representation of Discretely Sampled Surface Deformation for Displacement and Strain Analysis, *Exp. Mech.* **31**, 168 (1991) [324](#), [331](#), [332](#), [353](#)
8. T. C. Chu, W. F. Ranson, M. A. Sutton, W. H. Peters: Applications of Digital Image Correlation Techniques to Experimental Mechanics, *Exp. Mech.* **25**, 232 (1985) [324](#), [324](#), [331](#)
9. W. H. Peters, He Zheng-Hui, M. A. Sutton, W. F. Ranson: Two-Dimensional Fluid Velocity Measurements by Use of Digital Speckle Correlation Techniques, *Exp. Mech.* **24**, 117 (1984) [324](#), [324](#), [324](#)

10. S. R. McNeill, W. H. Peters, M. A. Sutton, W. F. Ranson: A Least Square Estimation of Stress Intensity Factor from Video-Computer Displacement Data, Proc. 12th Southeastern Conference of Theoretical and Applied Mechanics, (1984) p. 188 [324](#), [324](#), [324](#)
11. J. Anderson, W. H. Peters, M. A. Sutton, W. F. Ranson, T. C. Chu: Application of Digital Correlation Methods to Rigid Body Mechanics, Opt. Eng. **22**, 238 (1984) [324](#), [324](#), [324](#)
12. W. H. Peters, W. F. Ranson, J. F. Kalthoff, S. R. Winkler: A Study of Dynamic Near-Crack-Tip Fracture Parameters by Digital Image Analysis, J. Phys. IV Paris, Colloq **5**, suppl. n°8, Tome 46, 631 (1985) [324](#), [324](#)
13. W. Wu, W. H. Peters, M. Hammer: Basic Mechanical Properties of Retina in Simple Tension, Trans. ASME, J. Biomech. Eng. **109**, 1 (1987) [324](#), [324](#), [324](#)
14. S. R. McNeill, W. H. Peters, M. A. Sutton: Estimation of Stress Intensity Factor by Digital Image Correlation, Eng. Fract. Mech. **28**, 101 (1987) [324](#), [324](#), [324](#)
15. B. R. Durig, W. H. Peters, M. A. Hammer: Digital Image Correlation Measurements of Strain in Bovine Retina, in: *Optical Testing and Metrology*, Proc. SPIE **954**, 438 (1988) [324](#), [324](#), [324](#)
16. Y. J. Chao, M. A. Sutton: Measurement of Strains in a Paper Tensile Specimen Using Computer Vision and Digital Image Correlation, Part 1: Data Acquisition and Image Analysis System and Part 2: Tensile Specimen Test, Tappi J. **70** No.3, 173 and **70** No.4 153 (1988) [324](#), [324](#), [324](#), [325](#)
17. S. R. Russell, M. A. Sutton: Image Correlation Quantitative NDE of Impact and Fabrication Damage in a Glass Fiber Reinforced Composite System, J. Mater. Eval. **47**, 550 (1989) [324](#), [324](#)
18. S. R. Russell, M. A. Sutton, W. H. Peters: Strain Field Analysis Acquired through Correlation of X-ray Radiographs of Fiber-Reinforced Composite Laminates, Exp. Mech. **29**, 237 (1989) [324](#), [324](#)
19. W. H. Peters, W. M. Poplin, D. M. Walker, M. A. Sutton, W. F. Ranson: Whole Field Experimental Displacement Analysis of Composite Cylinders, Exp. Mech. **29**, 58 (1989) [324](#), [324](#), [324](#), [325](#)
20. B. Durig, H. Zhang, S. R. McNeill, Y. J. Chao, W. H. Peters: A Study of Mixed Mode Fracture by Photoelasticity and Digital Image Analysis, J. Opt. Lasers Engin. **14**, 203 (1991) [324](#), [324](#), [324](#)
21. C. Hurschler, J. T. Turner, Y. J. Chao, W. H. Peters: Thermal Shock of an Edge Cracked Plate: Experimental Determination of the Stress Intensity Factor by Digital Image Correlation, in: Proc. SEM Spring Conference on Experimental Mechanics, (1990) p. 374 [324](#), [324](#), [324](#)
22. M. A. Sutton, H. A. Bruck, T. L. Chae, J. L. Turner: Experimental Investigations of Three-Dimensional Effects Near a Crack-Tip Using Computer Vision, Int. J. Fract. **53**, 201 (1991) [324](#), [324](#), [324](#), [324](#), [325](#)
23. G. Han, M. A. Sutton, Y. J. Chao: A Study of Stable Crack Growth in Thin SEC Specimens of 304 Stainless Steel, Eng. Fract. Mech. **52**, 525 (1995) [324](#), [324](#), [324](#), [325](#)
24. G. Han, M. A. Sutton, Y. J. Chao: A Study of Stationary Crack-Tip Deformation Fields in Thin Sheets by Computer Vision, Exp. Mech. **34**, 357 (1994) [324](#), [324](#), [324](#), [324](#), [325](#)
25. D. S. Dawicke, M. A. Sutton: CTOA and Crack Tunneling Measurements in Thin Sheet 2024-T3 Aluminum Alloy, Exp. Mech. **34**, 357 (1994) [324](#), [324](#), [324](#), [325](#), [343](#), [344](#)

26. D. S. Dawicke, M. A. Sutton, J. C. Newman, C. A. Bigelow: Measurement and Analysis of Critical CTOA for an Aluminum Alloy Sheet, *ASTM STP 1220 on Fracture Mechanics* **25**, 358 (1995) [324](#), [324](#), [324](#), [325](#), [343](#)
27. S. R. McNeill, M. A. Sutton, Z. Miao, J. Ma: Measurement of Surface Profile Using Digital Image Correlation, *Exp. Mech.* **37**, 13 (1997) [324](#), [324](#), [325](#)
28. B. E. Amstutz, M. A. Sutton, D. S. Dawicke: Experimental Study of Mixed Mode I/II Stable Crack Growth in Thin 2024-T3 Aluminum, *ASTM STP 1256 on Fatigue and Fracture* **26**, 256 (1995) [324](#), [324](#), [325](#), [343](#), [344](#), [344](#), [344](#), [347](#)
29. D. J. Chen, F. P. Chiang, Y. S. Tan, H. S. Don: Digital Speckle-Displacement Measurement Using a Complex Spectrum Method, *Appl. Opt.* **32**, 1839 (1993) [325](#)
30. F. P. Chiang, Q. Wang, F. Lehman: New Developments in Full-Field Strain Measurements Using Speckles, *ASTM STP 1318 on Non-Traditional Methods of Sensing Stress, Strain and Damage in Materials and Structures*, 156 (1997) [325](#)
31. J. Liu, M. A. Sutton, J. S. Lyons: Experimental Characterization of Crack-Tip Deformations in Alloy 718 at High Temperatures, *J. Engr. Mat. Technol.* **120** (1998) [325](#)
32. J. S. Lyons, J. Liu, M. A. Sutton: Deformation Measurements at 650 °C with Computer Vision, *Exp. Mech.* **36**, 64 (1996) [325](#)
33. G. Vendroux, W. G. Knauss: Submicron Deformation Field Measurements: Part I, Developing a Digital Scanning Tunneling Microscope, *Exp. Mech.* **38**, 18 (1998) [325](#)
34. G. Vendroux, W. G. Knauss: Submicron Deformation Field Measurements: Part II, Improved Digital Image Correlation, *Exp. Mech.* **38**, 86 (1998) [325](#)
35. G. Vendroux, N. Schmidt, W. G. Knauss: Submicron Deformation Field Measurements: Part III, Demonstration of Deformation Determination, *Exp. Mech.* **38**, 154 (1998) [325](#)
36. S. Choi, S. P. Shah: Measurement of Deformations on Concrete Subjected to Compression Using Image Correlation, *Exp. Mech.* **37**, 304 (1997) [325](#)
37. L. Mott, S. M. Shaler, L. H. Groom: A Technique to Measure Strain Distributions in Single Wood Pulp Fibers. *J. Wood Fiber Sci.* **28**, 429 (1995) [325](#)
38. D. Choi: Failure Initiation and Propagation in Wood in Relation to its Structure, PhD thesis SUNY, Syracuse, NY (1991) [325](#)
39. D. Choi, J. L. Thorpe, R. B. Hanna: Image Analysis to Measure Strain in Wood and Paper, *Wood Sci. Technol.* **25**, 251 (1991) [325](#)
40. D. Choi, J. L. Thorpe, W. A. Cote, R. B. Hanna: Quantification of Compression Failure Propagation in Wood Using Digital Image Pattern Recognition, *J. Forest Prod.* **46**, 87 (1996) [325](#)
41. C. P. Agrawal: Full-field Deformation Measurements in Wood Using Digital Image Processing, MS thesis, Virginia Tech., Blacksburg, VA (1989) [325](#)
42. A. G. Zink, R. W. Davidson, R. B. Hanna: Strain Measurement in Wood Using a Digital Image Correlation Technique, *Wood Fiber Sci.* **27**, 346 (1995) [325](#)
43. A. G. Zink, R. B. Hanna, J. W. Stelmokas: Measurement of Poisson's Ratios for Yellow-Poplar, *J. Forest Prod.* **47**, 78 (1997) [325](#)
44. A. G. Zink, R. W. Davidson, R. B. Hanna: Effects of Composite Structure on Strain and Failure of Laminar and Wafer Composites, *Compos. Mater. Struct.* **4**, 345 (1997) [325](#)
45. G. Kifetew: Application of the Deformation Field Measurement Method on Wood During Drying, *Wood Sci. Technol.* **20**, 455 (1997) [325](#)

46. G. Kifetew, H. Lindberg, M. Wiklund M: Tangential and Radial Deformation Field Measurements on Wood During Drying, *Wood Sci. Technol.* **31**, 34 (1997) [325](#)
47. A. G. Zink, L. C. Pita: Strain Development in Wood During Kiln Drying, in: 52nd Annual Meeting of Forest Products Society, Mexico (1998) [325](#)
48. A. G. Zink, R. W. Davidson, R. B. Hanna: Experimental Measurement of the Strain Distribution in Double Overlap Wood Adhesive Joints, *J. Adhes.* **56**, 27 (1996) [325](#)
49. J. W. Stelmokas, A. G. Zink, J. L. Loferski: Image Correlation Analysis of Multiple Bolted Wood Connections, *Wood Fiber Sci.* **29**, 210 (1997) [325](#)
50. M. A. Sutton, W. Zhao, S. R. McNeill, J. D. Helm, W. Riddell, R. S. Piascik: Local Crack Closure Measurements; Development of a Measurement System Using Computer Vision and a Far-Field Microscope, in: 2nd International Symposium on Advances in Fatigue Crack Closure, San Diego, CA (1997) [325](#)
51. W. Riddell, R. S. Piascik, M. A. Sutton, W. Zhao, S. R. McNeill, J. D. Helm: Local Crack Closure Measurements: Determining Fatigue Crack Opening Loads from Near-crack-tip Displacement Measurements, in: 2nd International Symposium on Advances in Fatigue Crack Closure, San Diego, CA (1997) [325](#)
52. H. Lu, G. Vendroux, W. G. Knauss: Surface Deformation Measurements of a Cylindrical Specimen by Digital Image Correlation, *Exp. Mech.* **37**, 433 (1997) [326](#)
53. J. L. Thorpe, D. Choi, R. B. Hanna: Role Cockle, Following its Evolution, *TAPPI J.* **74**, 204 (1991) [326](#)
54. S. R. McNeill, M. Paquette: Initial Studies of Stereo Vision for Use in 3-D Deformation Measurements, unpublished internal report, Univ. South Carolina, SC (1988) [326](#)
55. P. F. Luo, Y. J. Chao, M. A. Sutton: Application of Stereo Vision to 3-D Deformation Analysis in Fracture Mechanics, *Opt. Eng.* **33**, 981 (1994) [326](#), [334](#), [343](#)
56. P. F. Luo, Y. J. Chao, M. A. Sutton: Accurate Measurement of Three-Dimensional Deformations in Deformable and Rigid Bodies Using Computer Vision, *Exp. Mech.* **33**, 123 (1993) [326](#), [334](#), [343](#)
57. P. F. Luo, Y. J. Chao, M. A. Sutton: Computer Vision Methods for Surface Deformation Measurements in Fracture Mechanics, *ASME-AMD Novel Experimental Methods in Fracture* **176**, 123 (1993) [326](#), [334](#), [343](#)
58. J. D. Helm, S. R. McNeill, M. A. Sutton: Improved 3-D Image Correlation for Surface Displacement Measurement, *Opt. Eng.* **35**, 1911 (1996) [326](#), [334](#), [338](#), [340](#), [341](#), [354](#)
59. J. D. Helm, M. A. Sutton, D. S. Dawicke, G. Hanna: Three-Dimensional Computer Vision Applications for Aircraft Fuselage Materials and Structures, in: 1st Joint DoD/FAA/NASA Conference on Aging Aircraft, Ogden, Utah (1997) [326](#), [340](#)
60. C. R. Dohrmann, H. R. Busby: Spline Function Smoothing and Differentiation of Noisy Data on a Rectangular Grid, in: *Proc. SEM Spring Conference Albuquerque, NM* (1990) p. 76 [332](#)
61. Z. Feng, R. E. Rowlands: Continuous Full-Field Representation and Differentiation of Three-Dimensional Experimental Vector Data, *Comput. Struct.* **26**, 979 (1987) [332](#)
62. J. D. Foley, A. van Dam, S. K. Feiner, J. F. Hughes: *Computer Graphics: Principles and Practice*, 2nd edn. Addison-Wesley, (1996) p. 1174 [332](#)

63. M. R. James, W. L. Morris, B. N. Cox, M. S. Dadkhah: Description and Application of Displacement Measurements Based on Digital Image Processing, ASME-AMD, Micromechanics: Experimental Techniques **102**, 89 (1989) [333](#)
64. D. Post: Moire' Interferometry: Its Capabilities for Micromechanics, ASME-AMD, Micromechanics: Experimental Techniques **102**, 15 (1989) [333](#)
65. J. McKelvie: Experimental Photomicromechanics: Fundamental Physics and Mathematical Contrivances, ASME-AMD, Micromechanics: Experimental Techniques **102**, 1 (1989) [333](#)
66. J. R. Maclin: Commercial Airplane Perspective on Multi Site Damage, in: International Conference on Aging Aircraft and Structural Airworthiness (1991) [343](#)
67. C. E. Harris: NASA Aircraft Structural Integrity Program, NASA Report-No. TM-102637 (1990) [343](#)
68. B. E. Amstutz, M. A. Sutton, D. S. Dawicke, M. L. Boone: Effects of Mixed ModeI/II Loading and Grain Orientation on Crack Initiation and Stable Tearing in 2024-T3 Aluminum, ASTM STP 1296 on Fatigue and Fracture Mechanics **27**, 105 (1997) [343](#), [344](#), [344](#), [347](#)
69. M. A. Sutton, W. Zhao, M. L. Boone, A. P. Reynolds, D. S. Dawicke: Prediction of crack growth direction for mode I/II loading using small-scale yielding and void initiation/growth concepts, Int. J. Fract. **83**, 275 (1997) [344](#)
70. W. N. Sharpe Jr.: Crack-Tip Opening Displacement Measurement Techniques, in J. S. Epstein (Ed.): *Experimental Techniques in Fracture*, VCH Weinheim, (1993) p. 219 [348](#), [348](#)
71. D. Post, B. Han, P. Ifju: *High Sensitivity Moire*, Springer, Berlin, Heidelberg (1994) [348](#)
72. M. A. Sutton, W. Zhao, S. R. McNeill, J. D. Helm, R. S. Piascik, W. Riddell: Local Crack Closure Measurements: Development of a Measurement System Using Computer Vision and a Far-Field Microscope, ASTM STP on Advances in Fatigue Crack Closure Measurements and Analysis, in press [350](#)
73. W. Riddell, R. S. Piascik, M. A. Sutton, W. Zhao, S. R. McNeill, J. D. Helm: Local Crack Closure Measurements: Interpretation of Fatigue Crack Closure Measurement Techniques, ASTM STP on Advances in Fatigue Crack Closure Measurements and Analysis, in press [350](#)